

Generalized and multi-oscillation solitons in the Nonlinear Schrödinger Equation with quartic dispersion

Ravindra Bandara* Andrus Giraldo† Neil G.R. Broderick‡ Bernd Krauskopf§

Abstract

We study different types of solitons of a generalized nonlinear Schrödinger equation (GNLSE) that models optical pulses traveling down an optical waveguide with quadratic as well as quartic dispersion. A traveling-wave ansatz transforms this partial differential equation into a fourth-order nonlinear ordinary differential equation (ODE) that is Hamiltonian and has two reversible symmetries. Homoclinic orbits of the ODE that connect the origin to itself represent solitons of the GNLSE, and this allows us to study the existence and organization of solitons with advanced numerical tools for the detection and continuation of connecting orbits. In this way, we establish the existence of connections from one periodic orbit to another, called PtoP connections. They give rise to families of homoclinic orbits to either of the two periodic orbits; in the GNLSE they correspond to *generalized solitons* with oscillating tails whose amplitude does not decay but reaches a nonzero limit. Moreover, PtoP connections can be found in the energy level of the origin, where connections between this equilibrium and a given periodic orbit, called EtoP connections, are known to organize families of solitons. As we show here, EtoP and PtoP cycles can be assembled into different types of heteroclinic cycles that give rise to additional families of homoclinic orbits to the origin. In the GNLSE, these correspond to *multi-oscillation solitons* that feature several episodes of different oscillations in between their decaying tails. As for solitons organized by EtoP connections only, multi-oscillation solitons are shown to be an integral part of the phenomenon of truncated homoclinic snaking.

1 Introduction

Optical solitons exist in photonic waveguides, notably, in optical fibers, due to the balance between dispersion and the Kerr nonlinearity, and they have been the focus of many recent experimental [35, 9] and theoretical [37, 38, 39, 25, 1, 6] studies. In the first instance, the dispersion has been modeled with a quadratic term. However, it has recently been discovered that waveguides with only quartic dispersion may support solitons with oscillating tails, which are much narrower in a well defined way (in terms of how the amplitude relates to the width [9]). This discovery of quartic solitons has led to considerable interest in characterizing the interplay between quartic and quadratic dispersion and the types of solitons this may entail [2, 6, 37, 38, 39]. To set the stage, pulse propagation along a waveguide with quadratic and quartic dispersion is governed by the Generalized Nonlinear Schrödinger Equation (GNLSE)

$$\frac{\partial A}{\partial z} = i\gamma|A|^2A - i\frac{\beta_2}{2}\frac{\partial^2 A}{\partial t^2} + i\frac{\beta_4}{24}\frac{\partial^4 A}{\partial t^4} \quad (1)$$

for the complex pulse envelope $A(z, t)$; here β_2 and β_4 are the respective dispersion coefficients, and γ represents the strength of the Kerr nonlinearity, which is cubic.

Theoretical and numerical work on the partial differential equation (PDE) (1) has shown the persistence of a single-hump (pulse) soliton [39], and the existence of infinitely many solitons with different symmetry

*Department of Mathematics and Dodd-Walls Centre for Photonic and Quantum Technologies, The University of Auckland, Private Bag 92019, Auckland 1142, New Zealand (ravindra.bandara@auckland.ac.nz)

†School of Computational Sciences, Korea Institute for Advanced Study, Seoul 02455, Korea (agiraldo@kias.re.kr)

‡Department of Physics and Dodd-Walls Centre for Photonic and Quantum Technologies, The University of Auckland, Private Bag 92019, Auckland 1142, New Zealand (n.broderick@auckland.ac.nz)

§Department of Mathematics and Dodd-Walls Centre for Photonic and Quantum Technologies, The University of Auckland, Private Bag 92019, Auckland 1142, New Zealand (b.krauskopf@auckland.ac.nz)

properties and numbers of humps [6, 33] for $\beta_4 < 0$ and a range of positive and negative values of β_2 . These results are obtained by considering a traveling-wave ansatz, which transforms the PDE into a Hamiltonian and reversible system of ordinary differential equations (ODEs) [16, 17, 11]. For the GNLSE (1) with $A(z, t) = u(t)e^{i\mu z}$, one thus obtains the system of ODEs [6]

$$\frac{d\mathbf{u}}{dt} = \begin{pmatrix} u_2 \\ u_3 \\ u_4 \\ \frac{24}{\beta_4} \left(\frac{\beta_2}{2} u_3 + \mu u_1 - \gamma u_1^3 \right) \end{pmatrix}, \quad (2)$$

where $\mathbf{u} = (u_1, u_2, u_3, u_4) = \left(u, \frac{du}{dt}, \frac{d^2u}{dt^2}, \frac{d^3u}{dt^3} \right)$. System (2) is Hamiltonian (thus, also volume-preserving) with the energy function [6, 33]

$$H(\mathbf{u}) = u_2 u_4 - \frac{1}{2} u_3^2 - \left(\frac{6\beta_2 u_2^2 - 6\gamma u_1^4 + 12\mu u_1^2}{\beta_4} \right)$$

as conserved quantity. Moreover, the system of ODEs (2) has two reversibilities given by the transformations

$$R_1 : (u_1, u_2, u_3, u_4) \rightarrow (u_1, -u_2, u_3, -u_4), \quad (3)$$

$$R_2 : (u_1, u_2, u_3, u_4) \rightarrow (-u_1, u_2, -u_3, u_4) \quad (4)$$

with corresponding reversibility sections

$$\Sigma_1 = \{ \mathbf{u} \in \mathbb{R}^4 : u_2 = u_4 = 0 \} \quad \text{and} \quad (5)$$

$$\Sigma_2 = \{ \mathbf{u} \in \mathbb{R}^4 : u_1 = u_3 = 0 \} \quad (6)$$

that are (pointwise) invariant under R_1 and R_2 , respectively [16, 11, 34, 14]. Hence, if $\mathbf{u}(t)$ is a trajectory or solution of system (2) then both $R_1(\mathbf{u}(-t))$ and $R_2(\mathbf{u}(-t))$ are also solutions [11, 34, 14]. We say that $\mathbf{u}(t)$ is *symmetric* if it is invariant as a set under R_1 and/or R_2 . Furthermore, we make the following further distinction of its symmetry properties: we say that $\mathbf{u}(t)$ is

- *R_1 -symmetric* when it is invariant under only R_1 ; here, \mathbf{u} intersects Σ_1 transversally;
- *R_2 -symmetric* when it is invariant under only R_2 ; here, \mathbf{u} intersects Σ_2 transversally.
- *R^* -symmetric* when it is invariant under R_1 as well as R_2 ; here, \mathbf{u} intersects both Σ_1 and Σ_2 transversally.
- *non-symmetric* when it is not invariant (under either R_1 or R_2).

Furthermore, system (2) is equivariant under the state-space symmetry transformation

$$S : (u_1, u_2, u_3, u_4) \rightarrow (-u_1, -u_2, -u_3, -u_4),$$

which is a point reflection in the origin $\mathbf{0} = (0, 0, 0, 0)$ and given by $S = R_1 \circ R_2 = R_2 \circ R_1$. Notice that invariance of a solution $\mathbf{u}(t)$ under S does not necessarily imply R^* -symmetry; however, any R^* -symmetric solution is necessarily invariant under S .

Solitons of the GNLSE (1) are given by the u_1 -component of homoclinic orbits to the origin $\mathbf{0} = (0, 0, 0, 0)$ of system (2), as a result of the traveling-wave ansatz [6, 33]. Note that $\mathbf{0}$ is an equilibrium in the zero-energy level $H \equiv 0$ and, moreover, $\mathbf{0} \in \Sigma_1 \cap \Sigma_2$. Hence, when $\mathbf{0}$ is a saddle, homoclinic orbits to it (approaching $\mathbf{0}$ in both forward and backward time) may be R_1 -symmetric, R_2 -symmetric, R^* -symmetric or non-symmetric [6]. In this Hamiltonian setting, homoclinic orbits lie in the same energy level as the equilibrium, and they are the limits of a family of periodic orbits (which are locally parametrized by the energy H). Moreover, any homoclinic orbit is structurally stable; that is, it persists under changes of parameters — unless it undergoes a bifurcation). There has been extensive work on fourth-order, reversible, and Hamiltonian systems [16, 17, 11, 23, 14, 4, 15] to understand the mechanism in which homoclinic solutions arise and disappear as parameters are varied.

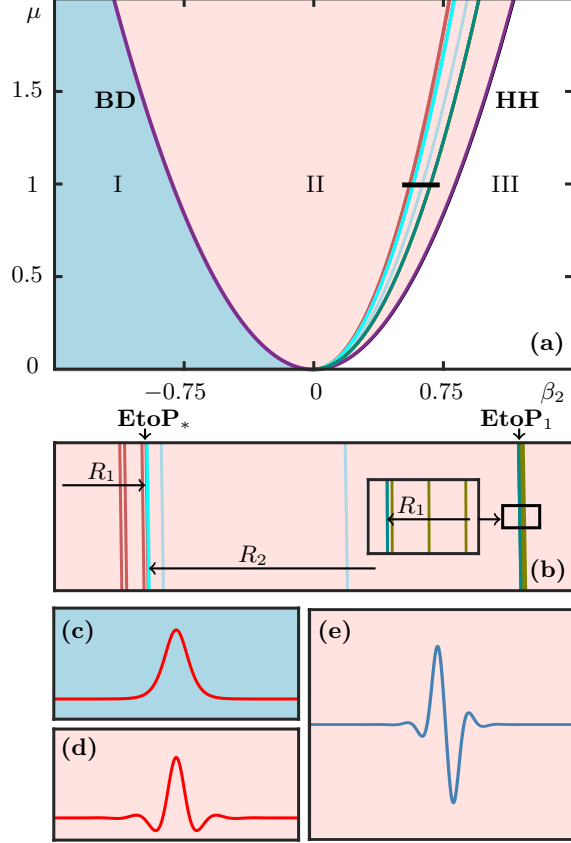


Figure 1: Panel (a) shows the bifurcation diagram of (2) in the (β_2, μ) -plane for $\beta_4 = -1$ and $\gamma = 1$ (a) with the curves **BD** and **HH** delimiting regions I (light blue), II (light green) and III (white); also shown in region II are fold curves of EtoP connections and associated solitons, whose ordering is illustrated in the enlargement panel (b). Panels (c) and (d) show the primary R_1 -symmetric homoclinic solution in region I for $(\beta_2, \mu) = (-1, 1)$ and for $(\beta_2, \mu) = (0.4, 1)$ in region II, respectively; panel (e) shows the primary R_2 -symmetric homoclinic solution in region II for $(\beta_2, \mu) = (0.4, 1)$.

System (2) is known [6, 37, 1] to have a pair of primary R_1 -symmetric homoclinic orbits to $\mathbf{0}$, which are each other's counterparts under the reversibility given by R_2 . The eigenvalues of the equilibrium $\mathbf{0}$ become complex conjugate while the pair of homoclinic orbits exists, and this is known as a Belyakov-Devaney (**BD**) bifurcation [16, 17]. Moreover, the primary homoclinic orbit disappears in a Hamiltonian Hopf (**HH**) bifurcation when $\mathbf{0}$ ceases to be a saddle and becomes a center. Without loss of generality, we may consider the (β_2, μ) -plane for $\beta_4 = -1$ and $\gamma = 1$ to find the relevant bifurcations, which all occur along semi-parabolas [6]. Figure 1(a) shows how the curves **BD** and **HH** together form a single (analytically known) parabola that divides the (β_2, μ) -plane into region I to III [6, 39]. In regions I and II the equilibrium $\mathbf{0}$ is a real saddle and a saddle-focus, respectively. The primary R_1 -symmetric homoclinic orbit exists in both these regions, and it is illustrated in panels (c) and (d) with temporal traces of u_1 that represent the corresponding soliton of the GNLSE (1). For simplicity we will refer to such u_1 -traces representing solitons as *homoclinic solutions* (as opposed to homoclinic orbits). Note that the soliton has non-oscillatory exponentially decaying tails in region I, and oscillating decaying tails in region II [6, 37, 1]. In region III, the equilibrium $\mathbf{0}$ is a center with purely imaginary eigenvalues and, hence, can no longer support homoclinic or other connecting orbits.

The Belyakov-Devaney bifurcation [16, 17] implies that infinitely many homoclinic solutions of different symmetry types exist to the right of the curve **BD** in Fig. 1(a) [6, 15]. Figure 1(e) shows the primary R_2 -symmetric homoclinic solution, which is special because it emerges from **BD** and exists throughout region II; that is, it disappears only at the Hamiltonian Hopf bifurcation curve **HH**. All other homoclinic orbits arise from **BD** as infinite families of different symmetry types, and they are associated with heteroclinic

connections between the equilibrium $\mathbf{0}$ and different periodic orbits, which we refer to as *EtoP connections*. The EtoP connections also persist under parameter variation; they come in pairs that disappear (as β_2 is increased) along curves, again parabolas, of fold bifurcations in region II, some of which are shown in Fig. 1(a). As we will discuss in more detail in Sec. 3, the associated homoclinic orbits of a given family also disappear in pairs at fold curves that are close to the fold curve of the corresponding EtoP connection [6]; the enlargement in Fig. 1(b) illustrates the ordering of these fold curves. We refer to the overall bifurcation structure as *BD-truncated homoclinic snaking* (as opposed to regular homoclinic snaking [41, 10]) and note that this phenomenon is also observed in a certain parameter regime of the Lugiato-Lefever equation [34].

In this paper, we establish the existence in the GNLSE (1) of heteroclinic connections between saddle periodic orbits in the same energy surface, which we refer to as *PtoP connections*. This type of connecting orbit also persists with parameters and plays an important role in the GNLSE for two main reasons. First of all, PtoP connections are organizing centers that ‘generate’ associated families of homoclinic orbits to saddle periodic orbits. Each such homoclinic orbit corresponds to a soliton with non-decaying periodic tails. This type of solution to a ‘periodic background’ is referred to as a *generalized soliton* in the context of optics [3]. Much like EtoP connections organize solitons with decaying tails, PtoP connections are shown to give rise to infinite families of generalized solitons with different symmetry properties.

Secondly, PtoP connections can be found in the zero-energy level. This allows us to combine them with EtoP connections to obtain heteroclinic cycles that, in turn, give rise to additional infinite families of solitons with decaying tails. These solitons are characterized by the corresponding homoclinic orbits ‘visiting’ not just one but several periodic orbits: they follow an EtoP connection from $\mathbf{0}$ to a periodic orbit, perform a certain number of oscillations near it, then follow a PtoP connection to another periodic orbit, perform a certain number of oscillations near it, possibly follow another PtoP connection, and so on, until they finally return to $\mathbf{0}$ via another EtoP connection. In contrast to the solitons considered before [6], which visit a single periodic orbit, we refer to these solitons organized by PtoP connections as *multi-oscillation solitons*. As we will show, they are also created at **BD**, may have different symmetry properties, and disappear in fold bifurcations before **HH** is reached. Hence, multi-oscillation solitons are an integral part of the phenomenon of BD-truncated homoclinic snaking in system (2).

Similarly, PtoP connections in the zero-energy surface arise in pairs from the Belyakov-Devaney bifurcation **BD** and disappear in fold bifurcations before **HH** is reached. Each such pair of PtoP connections gives rise to infinite families of homoclinic orbits of different symmetry properties to (each of) the two periodic orbits involved. In other words, we also find BD-truncated homoclinic snaking of homoclinic orbits to periodic orbits that are organized by corresponding PtoP connections. This phenomenon for homoclinic orbits to periodic orbits, which has not been reported previously in the literature, effectively generalizes BD-truncated homoclinic snaking of homoclinic orbits to equilibria [6, 34]. On the other hand, PtoP connections are not confined to the zero-energy level, and they form surfaces in phase space. We compute and present such surfaces, and this provides a connection to theoretical results on the existence of surfaces of homoclinic solutions to periodic solutions in reversible systems [22].

Clearly, PtoP connections require and go hand-in-hand with periodic orbits that they connect. Periodic orbits also form surfaces in phase space that are locally parametrized by the Hamiltonian function of the ODE [16, 17]. A central role in the overall organization of connecting orbits is played by the families of the periodic orbits that have as limits the pair of primary homoclinic orbits. Initially, for β_2 in region II and not too far from the curve **BD** in Fig. 1(a), there are three disjoint basic surfaces of periodic solutions. We compute these surfaces and show that they each intersect the zero-energy level infinitely many times. The overall picture of the soliton structure of the GNLSE (1) that therefore emerges is that the pair of primary homoclinic orbits generates infinitely many saddle periodic orbits in the zero-energy level. Sufficiently close to **BD** in region II, each such periodic orbit generates a pair of EtoP connections of $\mathbf{0}$. Moreover, any two periodic orbits in the zero-energy level can be connected by a pair of PtoP connections, which generate infinite families of homoclinic orbits to either of the periodic orbits. Concatenating any pair of EtoP connections with any number of PtoP connections creates infinitely many heteroclinic cycles from and to $\mathbf{0}$, each of which generates an entire menagerie of additional and arbitrarily complicated homoclinic orbits to the origin — and, hence novel types of solitons of the GNLSE. In turn, each homoclinic orbit is the limit of families of periodic orbits, infinitely many of which lie in the zero-energy level so that they also generate pairs of EtoP and PtoP solutions and so on.

The work presented here makes heavy use of state-of-the-art computational methods that allow us to find

different periodic, homoclinic and heteroclinic orbits, to continue them in parameters and to detect their bifurcations. In particular, we formulate connecting orbits between saddle objects as solutions of suitably defined two-point boundary value problems (2PBVPs) [30, 6]. In an approach called Lin’s method [31], this involves finding intersections of computed parts of stable and unstable manifolds of equilibria and periodic orbits in a three-dimensional section. Since system (2) is Hamiltonian, it is necessary to ensure that solutions to the respective 2PBVPs are isolated, which is achieved by introducing the gradient of the conserved quantity H multiplied with a perturbation parameter [21, 6] to system (2). All these computations are performed with the continuation package AUTO-07P [18] and its extension HOMCONT [13].

The paper is structured as follows. In Sec. 2, we introduce the three basic surfaces \mathcal{S}_1^\pm and \mathcal{S}_* of periodic orbits that accumulate on the primary homoclinic orbit and its R_2 -counterpart. In Sec. 3, we then briefly summarise previous results [6] regarding how EtoP connections to specific periodic orbits in these surfaces organize associated families of homoclinic orbits to $\mathbf{0}$; here, we also show a one-parameter bifurcation diagram that clarifies over which β_2 -ranges they exist. This sets the stage for the discussion in Sec. 4 of PtoP connections and how they generate generalized solitons. We first consider PtoP connections in the zero-energy, where they exist, and how they organize corresponding families of homoclinic orbits with different symmetry properties. We also calculate and present the surfaces of these PtoP connections, which are not restricted to have zero energy. We then provide in Sec. 5 a schematic diagram that shows how EtoP and PtoP connections can be concatenated into heteroclinic cycles. Specifically, we show how families of homoclinic orbits to $\mathbf{0}$ with different symmetry properties are generated by combining different EtoP and PtoP connections. These additional types of homoclinic orbits are indeed multi-oscillation solitons of the GNLSE, and one-parameter bifurcation diagrams show their β_2 -ranges of existence. We conclude in Sec. 6 with a brief summary and an outlook on open questions and future research.

2 The surfaces of basic periodic orbits

The primary homoclinic orbit from Fig. 1 is R_1 -symmetric but not R_2 -symmetric, meaning that it has an R_2 -counterpart. As is illustrated in Fig. 2, for $\beta_2 = 0.4$, this pair of primary homoclinic solutions gives rise to three basic surfaces; here and throughout, we fix, without loss of generality, $\beta_4 = -1$ and $\gamma = 1$, and set $\mu = 1$ since all bifurcation curves in the (β_2, μ) -plane are parabolas; note here that Eq. (1) can be rescaled appropriately for different signs of β_2 and β_4 , as was shown previously [6]. Figure 2(a1) shows the pair of primary homoclinic orbits in terms of their u_1 -profile, while panel (a2) shows them in the (u_1, u_2) -plane. They each come with a surface of periodic orbits that accumulates on the respective homoclinic orbit in the zero-energy level. These two surfaces \mathcal{S}_1^- and \mathcal{S}_1^+ are shown in projection onto (u_1, u_2, H) -space in panels (b) and (c), respectively. The parametrization by the energy H is explicit, and this allows us to easily identify the periodic orbits in the zero-energy level, which contains the origin $\mathbf{0}$ and the pair of primary homoclinic orbits, which are also shown in Fig. 2(b) and (c). Note that \mathcal{S}_1^- and \mathcal{S}_1^+ are both R_1 -symmetric and R_2 -counterparts of one another [6]. Moreover, they each extend over only a bounded range of H , where the largest value of H occurs at the equilibria \mathbf{E}^- and \mathbf{E}^+ . These are centers at $\mathbf{E}_\pm = \left(\pm\sqrt{\frac{\mu}{\gamma}}, 0, 0, 0\right)$ (so only exists if $\mu\gamma > 0$) and each others R_2 -counterparts with $H(\mathbf{E}_\pm) = -6\mu^2/(\gamma\beta_4)$. The union of the pair of primary homoclinic orbits is the limit of a third, R_* -symmetric surface \mathcal{S}_* , which is also shown in (u_1, u_2, H) -space in Fig. 2(d) together with the pair of primary homoclinic orbits. This surface has a maximal value of H but extends to arbitrarily large negative values of H ; that is, it is not bounded from below [6].

We refer to the the surfaces \mathcal{S}_1^\pm and \mathcal{S}_* as the surfaces of *basic periodic orbits*, and they are shown together in Fig. 3 in projections onto (u_1, u_2, H) -space, namely in a cutaway view that shows their parts for $u_2 \leq 0$ up to the section $\Sigma = \{(u_1, 0, u_3, u_4)\}$ defined by $u_2 = 0$. Notice that the respective other half, for positive u_2 on the other side of Σ , is obtained from that shown by applying the transformation R_1 . In Fig. 3, this corresponds to a reflection in the Σ -plane; compare with Fig. 2(b)–(d).

This cutaway representation allows us to compute and show the intersection curves of the surfaces \mathcal{S}_1^\pm and \mathcal{S}_* with the plane Σ , which is very useful for understanding the geometry of these surfaces. The gray line in Σ indicates the zero-energy level with $u_2 = 0$, which contains the basic homoclinic orbits. As Fig. 3 illustrates, the basic surfaces \mathcal{S}_1^\pm and \mathcal{S}_* each spiral as they limit on the (union of) the two basic homoclinic orbits, which means that they intersect the zero-energy level infinitely many times. To be more specific, starting from the equilibria \mathbf{E}_\pm and decreasing the energy H , one encounters in the zero-energy level the

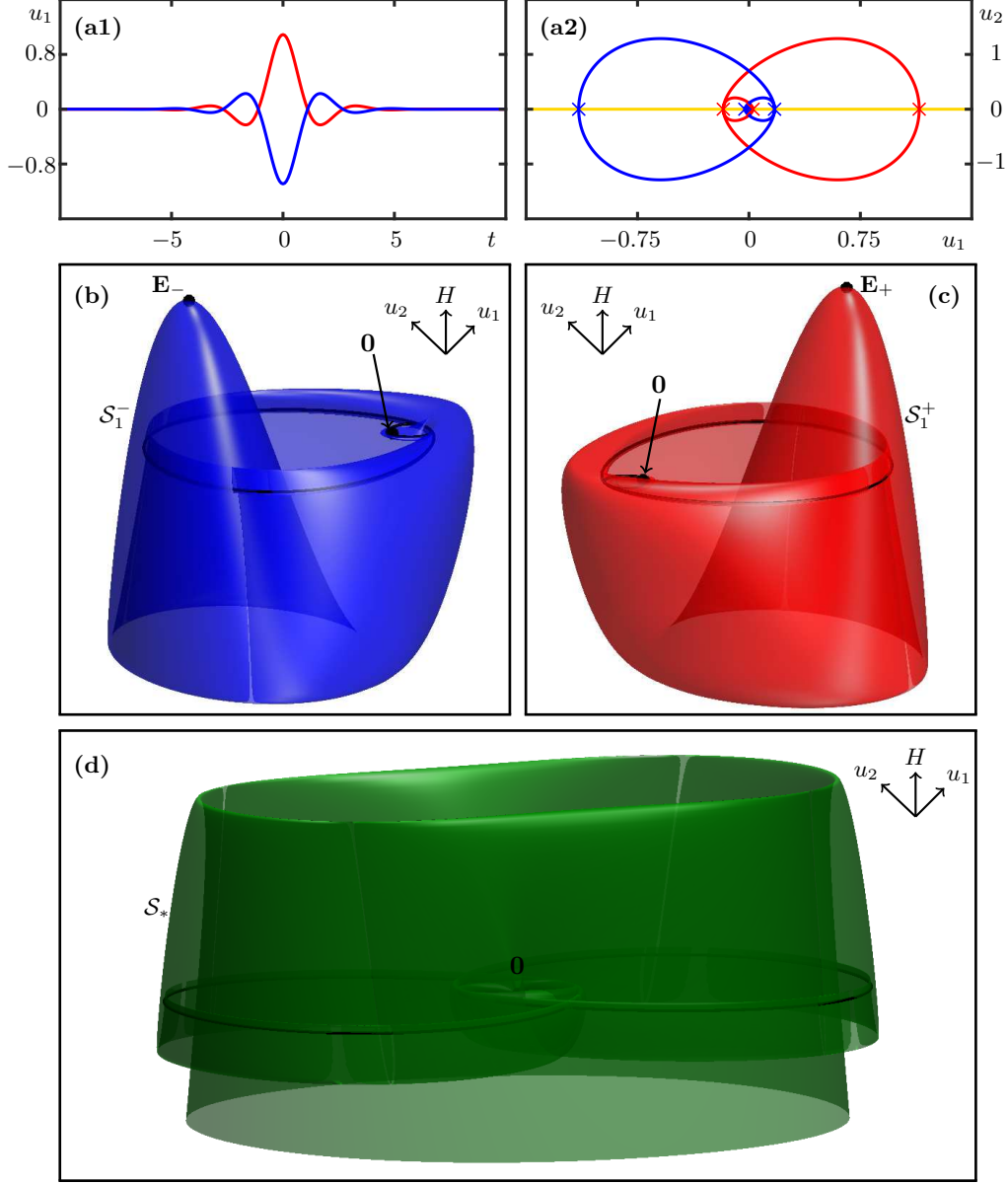


Figure 2: The primary R_1 -symmetric homoclinic orbit to $\mathbf{0}$ (red) and its R_2 -counterpart (blue) of system (2) for $\beta_2 = 0.4$, shown in panel (a1) as temporal profiles of the u_1 -component and in projection onto the (u_1, u_2) -plane, respectively. They are shown in (u_1, u_2, H) -space with the respective surfaces of periodic orbits, namely, \mathcal{S}_1^- (blue) with equilibrium \mathbf{E}_- in panel (b), \mathcal{S}_1^+ (red) with equilibrium \mathbf{E}_+ in panel (c), and \mathcal{S}_* (green) in (u_1, u_2, H) -space in panel (d). Throughout, the other parameters are set to $(\beta_4, \gamma, \mu) = (-1, 1, 1)$.

R_1 -symmetric and R_2 -related pair of periodic orbits Γ_1^- on \mathcal{S}_1^- and Γ_1^+ on \mathcal{S}_1^+ . Similarly, starting from large negative H and increasing the energy, one encounters in the zero-energy level the R_* -symmetric periodic orbit Γ_* on \mathcal{S}_* . The three periodic orbits Γ_1^\pm and Γ_* are shown in full in Fig. 3. As can be seen, they are the ‘first’ periodic orbits one encounters in the zero-energy level as the respective surface accumulates on the pair of homoclinic orbits. For this reason, we refer to Γ_1^\pm and Γ_* as the *primary periodic orbits*; note, in particular, that each of them is a single-loop orbit with exactly two intersection points with the section Σ .

In this work, we demonstrate with the specific examples of the primary periodic orbits Γ_1^\pm and Γ_* for $\beta_2 = 0.4$ how connecting orbits between them give rise to PtoP connection, which in turn generate generalized and multi-oscillation solitons. Indeed, the same is true for the further periodic orbits of \mathcal{S}_1^\pm and \mathcal{S}_* with

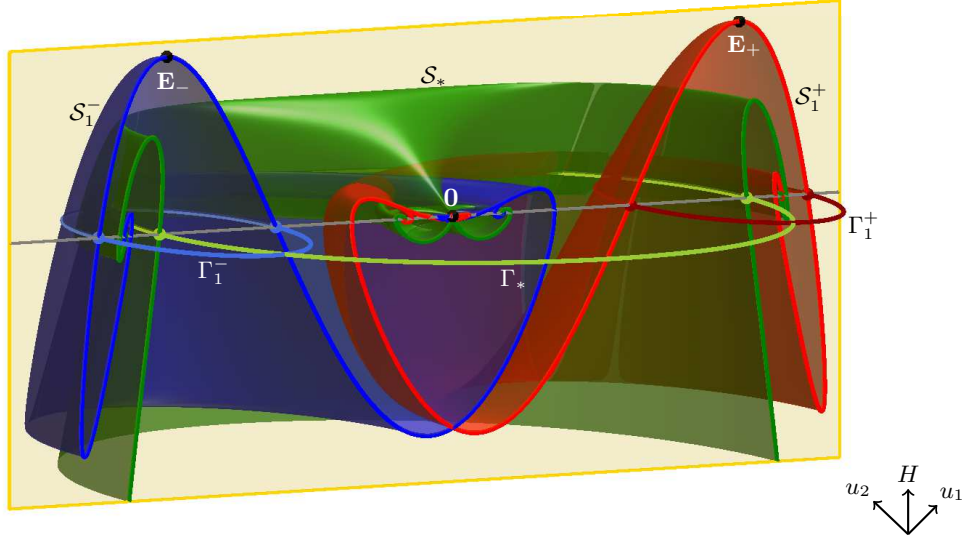


Figure 3: The surfaces \mathcal{S}_* , \mathcal{S}_1^- and \mathcal{S}_1^+ from Fig. 2(b)–(d), shown in a cutaway view in (u_1, u_2, H) -space up to the plane Σ where $u_2 = 0$; also shown are the equilibria $\mathbf{0}$ and \mathbf{E}_\pm (black dots), the zero-energy level (grey line) in Σ , and the primary periodic orbits Γ_1^- (blue curve), Γ_1^+ (red curve) and Γ_* (green curve) in the zero-energy level.

$H = 0$, of which there are countably infinitely many. In contrast to the primary periodic orbits, further periodic orbits of \mathcal{S}_1^\pm and \mathcal{S}_* in the zero-energy level are multi-loop orbits with an increasing number of additional intersection points with the (three-dimensional) section Σ . How they arise from the associated structure of \mathcal{S}_1^\pm and \mathcal{S}_* , and how these surfaces depend on the parameter β_2 are interesting subjects beyond the scope of this paper that will be discussed elsewhere [7].

3 EtoP cycles and their associated solitons

As a starting point for our introduction of PtoP orbits, we briefly recall and discuss here what families of solitons of different symmetry types are generated in region II by EtoP connections from $\mathbf{0}$ to the primary periodic orbits Γ_1^\pm and Γ_* [6], again for $\beta_2 = 0.4$ (and $\mu = 1$). The dependence of the EtoP connections and associated solitons on β_2 is subsequently presented as a one-parameter bifurcation diagram, which introduces the different fold curves already shown in Fig. 1.

Figures 4 and 5 show how the EtoP connections to Γ_* and to Γ_1^\pm , together with their corresponding symmetric counterparts, generate heteroclinic cycles that organize homoclinic orbits to $\mathbf{0}$ under mild conditions [32, 12, 6, 33]. These homoclinic orbits closely follow an EtoP connection and make a number of loops around the respective periodic orbit before converging back to $\mathbf{0}$ along a return EtoP connection. Homoclinic orbits with any number of loops can be found, and they form infinite families with increasing numbers of ‘humps’ of the corresponding solitons. Since system (2) possesses two reversible symmetries, families of homoclinic orbits with different symmetry properties can be obtained through this mechanism.

Figure 4 shows the EtoP connections to the primary periodic orbit Γ_* and associated homoclinic solutions. Panels (a) and (b) show two EtoP connections from $\mathbf{0}$ to Γ_* that exist simultaneously for $\beta_2 = 0.4$. Here, panels (a1) and (b1) show the EtoP connections in (u_1, u_2, H) -space together with a cutaway view of the surface \mathcal{S}_* ; and panels (a2) and (b2) show their u_1 -traces, which illustrates that the EtoP connections converge backward in time to $\mathbf{0}$ and forward in time to Γ_1^+ . Note that these two EtoP connections are distinct in the sense that they are not related by any of the symmetries of (2). However, since Γ_* is R^* -symmetric, the R_1 -counterparts as well as the R_2 -counterparts of these two EtoP connections exist as well. Note, in particular, that the R_2 -counterparts provide return connections from Γ_* to $\mathbf{0}$. Hence, the EtoP connections in Fig. 4(a) and (b) together with their corresponding R_1 - and R_2 -counterparts generate R_1 -

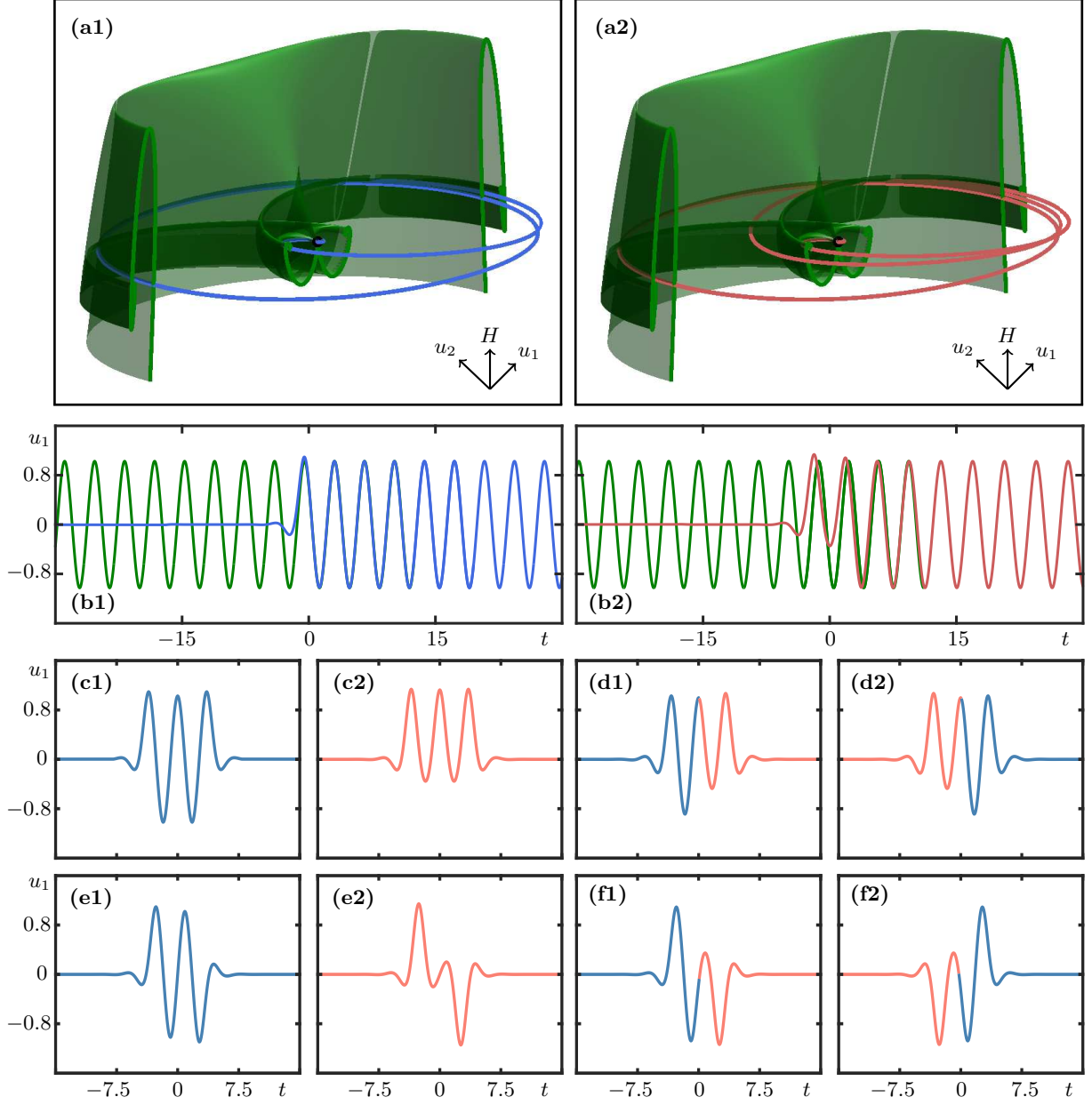


Figure 4: Homoclinic solutions associated with the basic R_* -symmetric periodic orbit Γ_* for $\beta_2 = 0.4$. Panels (a1) and (b1) show two distinct EtoP connections to Γ_* in (u_1, u_2, H) -space with a cutaway view of the surface \mathcal{S}_* ; and panels (a2) and (b2) show their u_1 -traces. Panels (c1), (c2) and (d1), (d2) show selected R_1 -symmetric and R_1 -symmetry-broken homoclinic solutions; and panels (e1), (e2) and (f1), (f2) show selected R_2 -symmetric and R_2 -symmetry-broken homoclinic solutions. Different coloring indicates the parts of the homoclinic orbits that are close to the respective EtoP connection (or its image under R_1 or R_2).

symmetric and R_1 -symmetry-broken, as well as R_2 -symmetric and R_2 -symmetry-broken homoclinic orbits, respectively [6]. Some representative examples are shown in Fig. 4(c)–(f) in terms of their u_1 -traces, where we distinguish by color the two parts that follow a particular EtoP connection (or its symmetric counterpart). More specifically, panels (c1) and (c2) show solutions with R_1 -symmetry that are generated from each of the two EtoP connections and their R_1 -counterparts; here, each EtoP connection is effectively followed to its second maximum. Similarly, an EtoP connection and then the R_1 -counterpart of the other combine to the

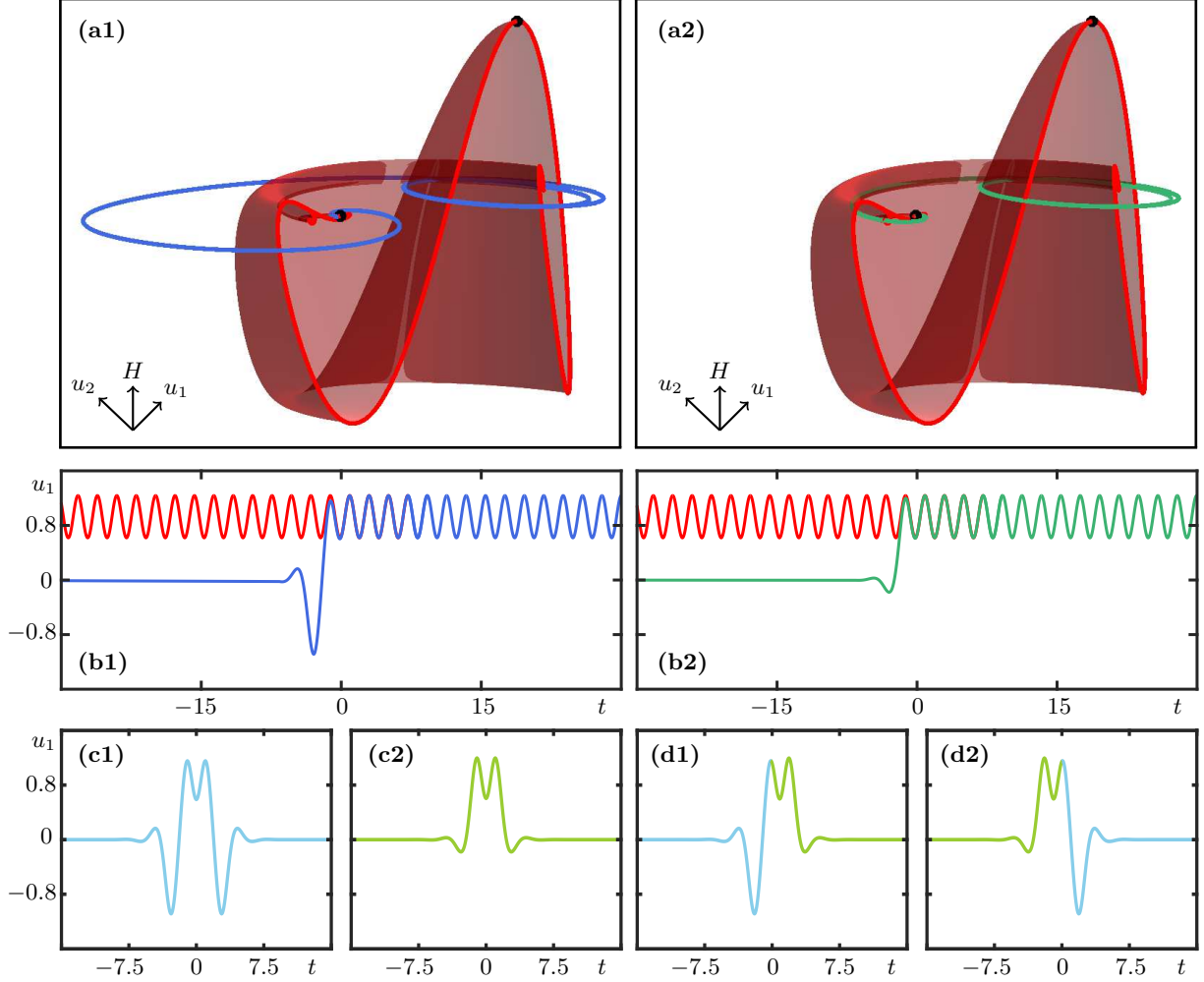


Figure 5: Homoclinic solutions associated with the primary R_1 -symmetric periodic orbit Γ_1^+ for $\beta_2 = 0.4$. Panels (a1) and (b1) show the two distinct EtoP connections to Γ_1^+ in (u_1, u_2, H) -space with a cutaway view of the surface \mathcal{S}_1^+ ; and panels (a2) and (b2) show their u_1 -traces. Panels (c1), (c2) and (d1), (d2) show selected R_1 -symmetric and R_1 -symmetry-broken homoclinic solutions, respectively. Different coloring indicates the parts of the homoclinic orbits that are close to the respective EtoP connection (or its image under R_1).

R_1 -symmetry-broken homoclinic solutions shown in panels (d1) and (d2). In complete analogy, panels (e1) and (e2) show homoclinic orbits with R_2 -symmetry that are generated from each of the two EtoP connections and their R_2 -counterparts. Combining an EtoP connection with the R_2 -counterpart of the other gives the R_2 -symmetry-broken homoclinic orbits shown in panels (f1) and (f2). We remark that the images of these solitons under the reversibility transformations given by R_1 and R_2 also exist; in the representation of the u_1 -trace in Fig. 4(c)–(f), these transformations are geometrically: reflection in the u_1 axis, and rotation by π around the origin of the (t, u_2) -plane, respectively.

In the same style, Fig. 5 shows the EtoP connections to Γ_1^+ and associated homoclinic solutions that exist simultaneously. The difference is now that Γ_1^+ is not R_2 -symmetric, and this means that the two distinct EtoP connections to Γ_1^+ , which are shown in panels (a) and (b) with a cutaway view of \mathcal{S}_1^+ , can only be combined with their R_1 -counterparts to generate heteroclinic cycles between $\mathbf{0}$ and Γ_1^+ . (Of course, their images under the reversibility R_2 also exist, but they are heteroclinic cycles between $\mathbf{0}$ and Γ_1^- .) Panels (c1) and (c2) of Fig. 5 show examples of R_1 -symmetric solitons that follow the respective EtoP connection to the first minimum near Γ_1^+ , and then follow the R_1 -counterpart back to $\mathbf{0}$. In contrast, the solitons shown in panels (d1) and (d2) are composed by each of the EtoP connections in combination with the R_1 -counterpart

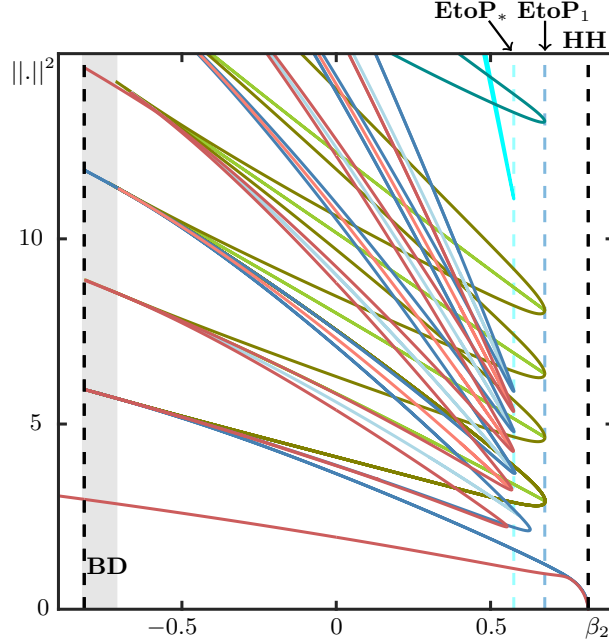


Figure 6: One-parameter bifurcation diagrams in β_2 of the families of homoclinic orbits associated with branches of the EtoP connections to Γ_* (cyan) and to Γ_1^+ (maroon). Shown are branches of R_1 -symmetric (dark red), R_1 -symmetry-broken (light red), R_2 -symmetric (dark blue) and R_1 -symmetry-broken (light blue) solitons with oscillations near Γ_* ; and R_1 -symmetric (dark green) and R_1 -symmetry-broken (light green) solitons with oscillations near Γ_1^+ ; compare with Figs. 4 and 5. The vertical dashed lines indicate the bifurcations **BD** and **HH**, and the fold points **EtoP*** and **EtoP₁** of the curves of EtoP connections to Γ_* and Γ_1^+ , respectively.

or the other EtoP connection, and this yields R_1 -symmetry-broken solitons.

Because system (2) is reversible and Hamiltonian, all connecting orbits, the EtoP connections and associated homoclinic orbits, persist in open regions of parameter space [11, 20]. Hence, once found, each such object can be continued as a solution branch in a chosen parameter, which we take to be the strength β_2 of the quadratic dispersion. In this way, one can compute a one-parameter bifurcation diagram that summarizes over what ranges of β_2 which types of connections and associated solitons can be found [6]. Figure 6 shows this kind of bifurcation diagram for the EtoP connections and different symmetric and symmetry-broken homoclinic orbits from Figs. 4 and 5. Here the shown β_2 -range includes the entire region II bounded by the bifurcations **BD** and **HH**, which are indicated by vertical lines and lie at $\beta_2 \approx \pm 0.8164$ (for $\mu = 1$). The different branches are represented by their L_2 -norm $\|\cdot\|^2$, which is computed as an integral over the respective computed (part of the) connecting orbit [18]. The L_2 -norm is a good choice to represent and distinguish branches of solitons because it increases with the number of maxima of the corresponding homoclinic orbits.

As Fig. 6 shows, the two EtoP connections to Γ_* from Figs. 4(a) and (b) lie on branches that emerge from **BD** and meet at a fold point at $\beta_2 \approx 0.5753$ to form a single smooth curve. The location of this fold, which we refer to as **EtoP***, is highlighted in Fig. 6 by a vertical dashed line. The primary R_1 -symmetric homoclinic orbit exists throughout regions I and II, forming a single branch that crosses **BD** and ends at **HH**. Note from Fig. 1(d) that, in region II, it can be interpreted as being part of the family of R_1 -symmetric homoclinic orbits that are close to an EtoP cycle between $\mathbf{0}$ and Γ_* . The other homoclinic orbits of this family, with more and more maxima as in Fig. 4(c), lie on branches that start at **BD** and meet in pairs at fold points to form smooth curves. In fact, these folds are points of symmetry breaking: they are also fold points where corresponding branches of R_1 -symmetry-broken homoclinic orbits, as those in Fig. 4(d), meet to form single curves from and back to **BD**. Four curves of each family are shown in Fig. 6; note that two simultaneously existing symmetry-broken solutions have the same L_2 -norm, which is why their two branches cannot be distinguished in Fig. 6. The situation for the families of R_2 -symmetric and R_2 -symmetry-broken

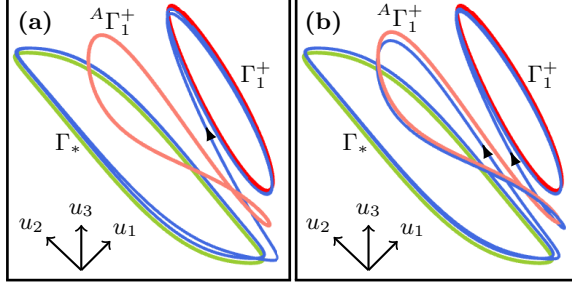


Figure 7: Pair of PtoP connections (blue curves) between Γ_* (green curve) to Γ_1^+ (red curve) of system (2) for $\beta_2 = 0.4$. Panels (a) and (b) show each of the PtoP connections in (u_1, u_1, u_3) -space, where the arrows indicate the direction of time; also shown is the additional saddle periodic orbit ${}^A\Gamma_1^+$ (salmon curve) that also lies on the surface \mathcal{S}_1^+ .

homoclinic orbits is very similar. The primary R_2 -symmetric homoclinic orbit from Fig. 1(e) is created at **BD** and ends at **HH**, and it can be interpreted as being part of the family of R_2 -symmetric homoclinic orbits that follow an EtoP cycle between **0** and Γ_* . As Fig. 6 shows, all other R_2 -symmetric homoclinic orbits, such as those in Fig. 4(e), come in pairs that form single curves, which meet the curves of the corresponding pairs of R_2 -symmetry-broken homoclinic orbits, as those in Fig. 4(e), at their respective fold points. Again, four curves of these families are shown in Fig. 6, and they illustrate that the folds of the families of R_1 -symmetric and of the R_2 -symmetric homoclinic orbits converge to the fold **EtoP** $_*$, from the left and from the right, respectively; compare with Fig. 1(b).

Similarly, the two EtoP connections to Γ_1^+ from Figs. 5(a) and (b) (and also those to Γ_1^- by R_2 -symmetry) lie on a single branch that emerges from and returns to **BD**, with a fold point that lies at $\beta_2 \approx 0.6756$. We refer to this fold as **EtoP** $_1$, and it is also highlighted by a vertical dashed line in Fig. 6. For this type of R_1 -symmetric EtoP connection, there only exist R_1 -symmetric and R_1 -symmetry-broken homoclinic orbits that come in pairs, as those in Fig. 5(c) and (d). Their branches, of which four are shown in Fig. 6, meet in the same way at joint fold points. These fold points are very close to and converge to the fold **EtoP** $_1$ from the right; see Fig. 1(b).

4 PtoP connections and generalized solitons

We now show that one can find pairs of heteroclinic connections between two given saddle periodic orbits in the same energy level. More specifically, we compute and present such PtoP connections between the saddle periodic orbits Γ_* and Γ_1^+ , and show that they emerge from the Belyakov-Devaney bifurcation **BD** and exist over a considerable β_2 -range in region II.

Figure 7 shows in projection onto (u_1, u_1, u_3) -space a pair of PtoP connections between Γ_* and Γ_1^+ for $\beta_2 = 0.4$. Each of these two PtoP connections is clearly seen to converge backward in time to Γ_* and forward in time to Γ_1^+ , and they are not related by symmetry. While the PtoP connection in Fig. 7(a) transitions swiftly from Γ_* to Γ_1^+ , the one in panel (b) has almost a complete loop near and around a third saddle periodic orbit ${}^A\Gamma_1^+$ that also lies on the surface \mathcal{S}_1^+ . All objects shown in Fig. 7 lie in the zero-energy level.

As we discuss next, such pairs of PtoP connections give rise to families of homoclinic orbits, to either Γ_* or Γ_1^\pm in this case. In the GNLSE, they correspond to generalized solitons [3] with non-decaying periodic tails, which are not confined to the zero-energy level. In Sec. 5, we then show how PtoP connections in the zero-energy level can be combined with EtoP connections to form heteroclinic cycles from and back to **0** that generate families of multi-oscillation solitons.

4.1 Homoclinic orbits to Γ_*

Figure 8 shows families of homoclinic orbits associated with the PtoP connection between Γ_* and Γ_1^+ , specifically examples of solution profiles and the associated bifurcation diagram. The u_1 -traces of the two PtoP connections from Fig. 7 are shown in Figure 8(a), which illustrates further how they connect Γ_* and Γ_1^+ .

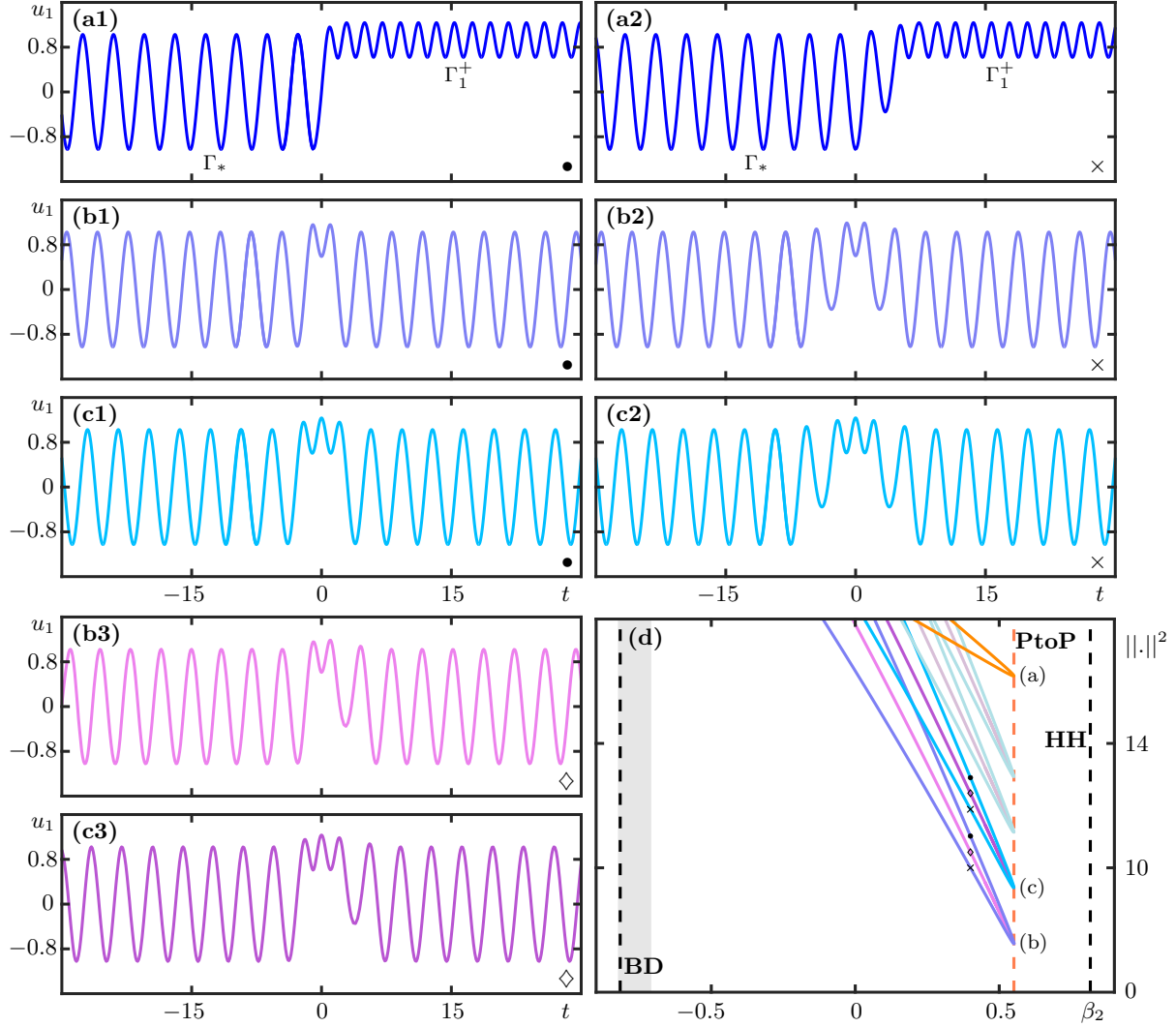


Figure 8: Pair of PtoP connections from Γ_* to Γ_1^+ and associated families of homoclinic solutions to Γ_* . Panels (a1) and (a2) show the two PtoP connections; panels (b1),(c1) and (b2),(c2) R_1 -symmetric, and panels (b3),(c3) R_1 -symmetry-broken homoclinic solutions to Γ_* . Panel (d) is the corresponding one-parameter bifurcation diagram in β_2 with the curve of PtoP connections (orange curve) and curves of homoclinic connections to Γ_* . The vertical dashed lines indicate **BD**, **HH** and the fold point **PtoP** of PtoP connections; the color of the bifurcation curves and the dots, crosses and diamonds indicate the locations of the solutions in panels (b1) and (c1), (b2) and (c2), and (b3) and (c3), respectively.

Notice the intermediate minimum in u_1 in panel (a2), which corresponds to the loop around the additional orbit ${}^A\Gamma_1^+$ in Fig. 7(b). Since both Γ_* and Γ_1^+ are R_1 -symmetric, the R_1 -counterparts of the PtoP connections in Figure 8(a), obtained by reflection in the u_1 -axis, also exist: they correspond to return connections from Γ_1^+ to Γ_* . Hence, the two connections shown in panels (a) and their corresponding R_1 -counterparts create different heteroclinic cycles between Γ_* and Γ_1^+ , and these organize different types of homoclinic solutions to Γ_* and to Γ_1^+ , respectively.

Panels (b) and (c) of Fig. 8 show examples of homoclinic orbits to Γ_* that are generated by PtoP cycles consisting of the two PtoP connections in Fig. 8(a) and their R_1 -counterparts. More specifically, the homoclinic solutions in panels (b1) and (c1) follow the PtoP connection in panel (a1) from Γ_* to near Γ_1^+ and then follow its R_1 -counterpart back to Γ_* . Those in panels (b2) and (c2) follow, similarly, the PtoP connection in panel (a2) and its R_1 -counterpart. Finally, panels (b3) and (c3) show non-symmetric homoclinic solutions

to Γ_* , which follow the PtoP connection in panel (a1) and the R_1 -counterpart of that in panel (a2). The difference between panels (b) and (c) is that these homoclinic solutions make one and two loops around Γ_1^+ , respectively. Indeed, by following the respective PtoP connections longer, homoclinic solutions to Γ_* with any number of loops around Γ_1^+ can be found.

Figure 8(d) shows the one-parameter bifurcation diagram in β_2 of the PtoP connections, as well as the R_1 -symmetric and non-symmetric homoclinic solutions to Γ_* , represented by the L_2 -norm $\|u_1\|^2$ of a suitably truncated portion of the solutions. As in Fig. 6, dashed vertical lines indicate the bifurcations **BD** and **HH** that bound the β_2 -range in region II where the equilibrium $\mathbf{0}$ is a saddle-focus. As is the case for the EtoP connections, the two PtoP connections in panels (a1) and (a2) lie on branches that emerge from **BD** and meet at a fold point to form a single curve. This fold, which we refer to as **PtoP**, occurs at $\beta_2 \approx 0.5511$ and this is also indicated by a vertical dashed line in Fig. 8(d); the PtoP connections in panels (a1) and (a2) are from the upper and the lower branch of this curve, respectively, and they no longer exist to the right of the line **PtoP**. We remark that the PtoP connections, which actually have an infinite L_2 -norm, are represented in panel (d) by the L_2 -norm of their truncation with ten loops near each periodic solution Γ_* and Γ_1^+ .

Also shown in Fig. 8(d) are the four branches of R_1 -symmetric and non-symmetric homoclinic solutions to Γ_* with up to four oscillations near Γ_1^+ . Since homoclinic connections to periodic orbits also have infinite L_2 -norm, they are also represented here by the L_2 -norm of a truncation, with four oscillations near Γ_* in this case. As was the case for branches of homoclinic orbits to $\mathbf{0}$ in Sec. 3, the different branches of increasing norm connect in pairs at fold bifurcation. More specifically, the R_1 -symmetric homoclinic solutions to Γ_* lie on branches that meet at fold points to form smooth curves. Here, the upper and lower branches represent homoclinic solutions generated by the PtoP connection in panel (a1) and its R_1 -counterpart, and that in panel (a2) and its R_1 -counterpart, respectively. The example solutions in panels (b1),(c1) and (b2),(c2) are indicated in Fig. 8(d) by dots and crosses on the correspondingly colored branches. Similarly, the non-symmetric homoclinic solutions to Γ_* lie on branches that meet at fold points, which are also the fold points of the corresponding R_1 -symmetric solutions with the same number of loops around Γ_1^+ . Hence, these folds are symmetry-breaking bifurcations of homoclinic orbits to Γ_* , which is why we refer to this family as R_1 -symmetry-broken. Note that the pairs of branches of symmetry-broken solutions are not distinguished by the norm and appear to be on top of each other in Fig. 8(d); the example solutions in panels (b3),(c3) are indicated in by diamonds on the correspondingly colored branches. As the number of loops around Γ_1^+ increases, the folds of the respective curves accumulate on the fold of PtoP connections from the left; notice that all these fold points have β_2 -values that are very close to one another: in fact, they agree up to four decimal places with the value $\beta_2 \approx 0.5511$ of **PtoP**.

4.2 Homoclinic orbits to Γ_1^+

PtoP cycles organize homoclinic solutions to any periodic solutions involved in the cycle. In particular, and as Fig. 9 shows, the pair of PtoP connections from Figs. 7 and 8(a) also generates families of homoclinic solutions to the periodic solution Γ_1^+ . Example solutions with one and two oscillations near Γ_* are shown in Fig. 9(a) and (b), and panel (c) is the associated bifurcation diagram that also includes the curve of PtoP connections. Comparison with Fig. 8(b)–(d) shows that the different families of R_1 -symmetric and R_1 -symmetry-broken homoclinic solutions are organized in the same way. Specifically, Fig. 9(a1) and (b1) show R_1 -symmetric homoclinic solutions that follow the R_1 -counterpart of the PtoP connection in Fig. 8(a1) from Γ_1^+ to near Γ_* and then follow this PtoP connection back to Γ_* . Figure 9(a2) and (b2) show the same type of homoclinic orbit, but now for the other PtoP connection, and panels (a3) and (b3) show the corresponding R_1 -symmetry-broken homoclinic solutions obtained from combining the two PtoP connections. The respective pairs of branches of homoclinic orbits with any number of loops around Γ_* , of which the first four are shown in Fig. 9(c), meet at fold points to form smooth curves; the locations of the different example solutions are again marked. The folds of the respective pairs coincide and are symmetry-breaking bifurcations of the homoclinic solutions to Γ_1^+ . As the number of loops around Γ_* increases, these fold points converge to the fold of the curve of PtoP connections; their β_2 -values are indistinguishable (up to the accuracy of the continuation) from the value $\beta_2 \approx 0.5511$ of the point **PtoP**.

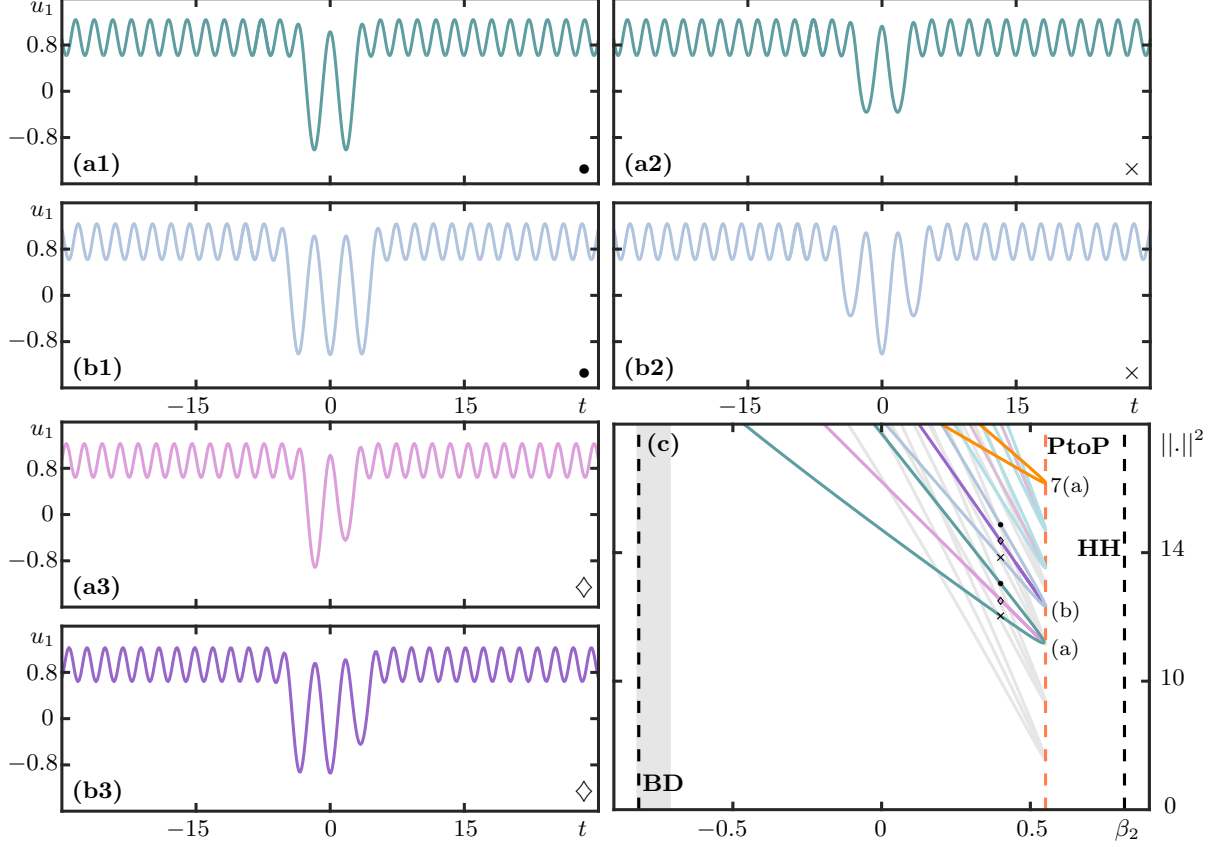


Figure 9: Families of homoclinic solutions to Γ_1^+ associated with the PtoP connections from Fig. 8(a). Panels (a1),(b1) and (a2),(b2) show R_1 -symmetric, and panels (a3) and (b3) R_1 -symmetry-broken homoclinic solutions to Γ_1^+ . Panel (c) is the corresponding one-parameter bifurcation diagram in β_2 with the curve of PtoP connections (orange curve) and curves of homoclinic connections to Γ_1^+ . The vertical dashed lines indicate **BD**, **HH** and the fold point **PtoP**; the color of the bifurcation curves and the dots, crosses and diamonds indicate the locations of the solutions in panels (a1) and (b1), (a2) and (b2), and (a3) and (b3), respectively.

4.3 BD-truncated snaking of generalized solitons

Figures 8(d) and 9(c) show how the PtoP connections from Figures 7 organize families of R_1 -symmetric and R_1 -symmetry-broken homoclinic solutions to either Γ^* and Γ_1^+ . For increasing β_2 , the curves of all these homoclinic solutions have folds, effectively all at the point **PtoP**, and disappear before reaching the bifurcation **HH**. Continuing these branches of homoclinic solutions to periodic orbits for decreasing β_2 turns out to be numerically more challenging. They have been computed to considerably lower values than shown in Figs. 8(d) and 9(c), where their L_2 -norm increases significantly for decreasing β_2 . Nevertheless, our numerical computations strongly suggest that the homoclinic solutions to Γ^* and Γ_1^+ are all also created at the Belyakov-Devaney bifurcation **BD**; however, this limit is not quite reached in the computation of the branches due to increased sensitivity of the continuations, which is arguably due to the oscillating nature of their tails.

Note that the R_2 -symmetric counterparts of the homoclinic solutions in Fig. 8(b1)–(c3) are also homoclinic solutions to Γ_* ; however, they now make multiple loops around Γ_1^- . Since they have the same L_2 -norm, their curves in the one-parameter bifurcation diagram are identical to those shown in panel (d). The R_2 -symmetric counterparts of the homoclinic solutions to Γ_1^+ in Fig. 9(a1)–(b3) are simply the corresponding homoclinic solutions to Γ_1^- . Again, these have the same L_2 -norm and so occur along the curves already shown in the bifurcation diagram in panel (c); hence, each curve represents homoclinic solutions both to Γ_1^+ and to Γ_1^- .

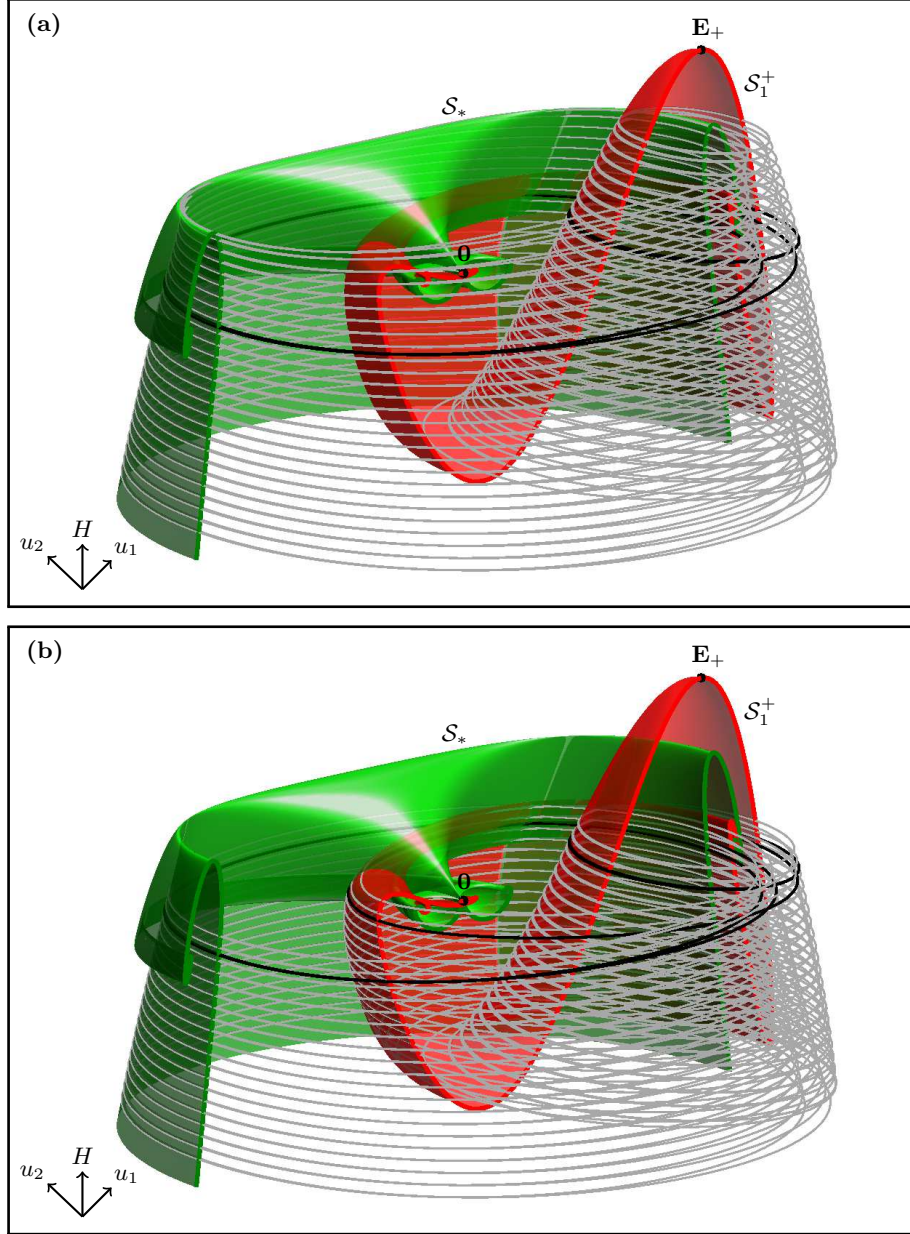


Figure 10: Pair of surfaces in (u_1, u_2, H) -space of PtoP connections of system (2) for $\beta_2 = 0.4$, shown with cutaway views of the surfaces \mathcal{S}_* (green) and \mathcal{S}_1^+ (red) of periodic orbits. Specifically, panels (a) and (b) show a representative number of PtoP connections (gray curves), equally distributed in H , of the respective one-parameter family obtained by continuation of the PtoP connections in the zero-energy surface (black curves) from Fig. 7(a) and (b).

All these families of homoclinic orbits to periodic orbits of the ODE system (2) are generalized solitons (with non-decaying tails) of the GNLSE (1). In other words, as for the regular solitons with decaying tails [6], we find that the generalized solitons are also organized by the phenomenon of BD-truncated homoclinic snaking, where the homoclinic orbits are now to periodic orbits rather than to the equilibrium $\mathbf{0}$; compare Figs. 8(d) and 9(c) with Fig. 6. An important difference is that BD-truncated homoclinic snaking to periodic orbits exists not only in the zero-energy level, as we will show next.

4.4 Surfaces of PtoP connections

Since Γ_* and Γ_1^+ lie in the zero-energy level, so do the PtoP connections in Fig. 7. However, the periodic orbits can be continued to obtain the surfaces \mathcal{S}_* and \mathcal{S}_1^+ from Fig. 2(c) and (d). As Fig. 10 shows, each of the two PtoP connections can similarly be continued in the energy H to PtoP connections of corresponding periodic orbits in the respective energy level of \mathcal{S}_* and \mathcal{S}_1^+ . Here, panels (a) and (b) show the surfaces \mathcal{S}_* and \mathcal{S}_1^+ in (u_1, u_2, H) -space, together with a number of representative PtoP connections of the corresponding one-parameter family; these are not rendered as a surface for clarity of presentation, and the PtoP connections from Fig. 7 are highlighted. Note that one could also continue each homoclinic solution in Fig. 8 and Fig. 9 to find their respective continuations in H . We rather continue here the two PtoP connections themselves because they organize the many homoclinic solutions to the periodic orbits in the surfaces \mathcal{S}_* and \mathcal{S}_1^+ . In this way, we present a global picture that allows one to make connections to theoretical results on the existence of surfaces of homoclinic solutions to periodic solutions in reversible systems [22].

Figure 10 clearly shows that the PtoP cycles and associated homoclinic orbits can be found over a range of the energy H ; specifically, over the range of the joint existence of the continuations of the periodic orbits Γ_* and Γ_1^+ . As we continue the PtoP connections in the zero-energy level (black curves) towards positive and negative values of H , they reach a maximum and a minimum energy level, respectively, which correspond to folds with respect to H of periodic orbits on the surfaces \mathcal{S}_* and \mathcal{S}_1^+ . We remark that these continuations are quite delicate near such local extrema of the energy, and it is difficult to continue a branch past such a fold. Nevertheless, we are able to identify the respective PtoP connection past the fold and resume the continuation in this way. More specifically, as we continue the PtoP connection in Fig. 7(a) towards the positive values of H , it reaches the energy level with $H \approx 3.3$, which is the global maximum of \mathcal{S}_* ; see Fig. 10(a). When we continue it towards negative values of H , it reaches the energy level with $H \approx -6.2$, which is the global minimum of \mathcal{S}_1^+ . Likewise, when the connection in Fig. 7(b) is continued towards negative values of H , it also reaches the energy level with $H \approx -6.2$; see Fig. 10(b). However, as we continue it towards positive values of H , it only reaches the energy level with $H \approx 0.29$. This is because this family of PtoP connections has an extra loop near the continuation of the R_1 -symmetric periodic orbit ${}^A\Gamma_1^+$ on \mathcal{S}_1^+ , which only exists up to the local maximum of \mathcal{S}_1^+ at energy level $H \approx 0.29$. The close passage of the PtoP connection in Fig. 7(b) of ${}^A\Gamma_1^+$ already demonstrates that it is possible to find PtoP connections between Γ_* and ${}^A\Gamma_1^+$ and between Γ_1^+ and ${}^A\Gamma_1^+$. Overall, past any fold on the surface \mathcal{S}_* or \mathcal{S}_1^+ the respective PtoP connection connects different periodic orbits, and they all exist over a certain range of H .

Any PtoP connections in a given energy level can be combined to create heteroclinic PtoP cycles between different periodic orbits and associated homoclinic orbits, that is, additional families of generalized solitons that exist over certain ranges of H near $H = 0$. In particular, there are infinitely many families of homoclinic orbits to the periodic orbits Γ_* and Γ_1^\pm in the zero-energy level. This geometric picture allows us to conclude the following. As Γ_* and/or Γ_1^\pm approach the primary homoclinic orbits in the zero-energy level, the families of the associated homoclinic orbits to the periodic orbits Γ_* and/or Γ_1^\pm approach connecting orbits from and back to the primary homoclinic orbits to $\mathbf{0}$. Taking the limit may, hence, be a mechanism for creating homoclinic orbits to homoclinic orbits, which are also referred to as super-homoclinic orbits [5]. These objects are limits of generalized solitons in the GNLSE, and it is an interesting question beyond the scope of this paper whether and how they act as organizing centers for the different types of solitons.

5 P_{to}P connections and multi-oscillation solitons

In the zero-energy level one finds the PtoP connections between Γ_* and Γ_1^+ from Fig. 7, as well as their R_1 - and R_2 -counterparts that involve Γ_1^- . Together they are involved in creating more complicated heteroclinic PtoP cycles between the three periodic orbits Γ_* , Γ_1^+ and Γ_1^- . As we show now, these PtoP cycles can be combined with the EtoP connections from Sec. 3 effectively in any combination to create more complicated heteroclinic cycles from and back to $\mathbf{0}$. In turn, these organize a plethora of homoclinic orbits to $\mathbf{0}$, which all correspond to solitons of the GNLSE with decaying tails that feature episodes of oscillations near any of these periodic orbits. For this reason, we refer to them as multi-oscillation solitons.

This whole mechanism is summarized in Fig. 11, which shows a schematic diagram in the form of a graph of possible connections between $\mathbf{0}$, Γ_* , and Γ^\pm at β_2 -values where all of them exist, such as for $\beta = 0.4$ as we used throughout. As we discussed in Sec 3 and Sec. 4, there exist two distinct EtoP and PtoP connections

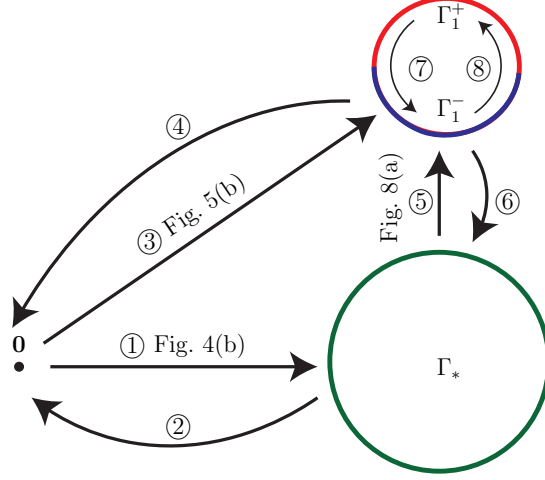


Figure 11: Schematic digram showcasing all the possible connections between $\mathbf{0}$ (black dot), Γ_* (green circle), and Γ_1^\pm (red/blue circle). Arrows indicate different EtoP and PtoP connections with reference to previous figures, and they are labeled ① to ⑧.

for fixed parameter values, and they are represented in Fig. 11 by single directed edges that are numbered ① to ⑧; here the arrows indicate the direction of time and reference to previous figures indicates already the encountered connections. The edges labeled ⑦ and ⑧ represent pairs of PtoP connections between the R_2 -counterparts Γ_1^+ and Γ_1^- , which are jointly represented by a single bi-colored circle. Furthermore, in this labeling, the even connections ②, ④, ⑥ and ⑧ correspond to the R_1 - or R_2 -counterparts of the odd connections ①, ③, ⑤ and ⑦, respectively.

Any path in the directed graph in Fig. 11 that starts and ends at $\mathbf{0}$ represents certain heteroclinic cycles with associated infinite families of homoclinic orbits to $\mathbf{0}$ of the different symmetry types, which are all solitons of the GNLSE. Notice that the families of homoclinic solutions that were previously found [6] and are summarized in Sec. 3 are organized by the cycles that are formed by only the connections ① and ②, and by ③ and ④. That is, they reach Γ_* or Γ_1^+ along the EtoP connection ① or ③, loop multiple type times close to the respective periodic orbit, and then converge back to $\mathbf{0}$ along the EtoP connection ② or ④. Importantly, the existence of the PtoP connections ⑤ to ⑧ that connect the periodic orbits Γ_* and Γ_1^\pm allows for more complicated homoclinic solutions to $\mathbf{0}$ to be constructed. Each arrow represents two distinct connections from one saddle object to another, which makes this mechanism more complex than Fig 11 suggests.

Our numerical evidence supports the observation/conjecture that for any path from $\mathbf{0}$ back to itself in Fig 11, the corresponding EtoP cycles with associated families of homoclinic solutions to $\mathbf{0}$ indeed exist in system (2). To illustrate this statement, we consider two specific paths and compute and show the corresponding families of homoclinic solutions. We first consider the heteroclinic cycles given by the edge sequence

$$\mathbf{0} \xrightarrow{\textcircled{1}} \Gamma_* \xrightarrow{\textcircled{5}} \Gamma_1^+ \xrightarrow{\textcircled{6}} \Gamma_* \xrightarrow{\textcircled{2}} \mathbf{0},$$

which we say is of type ((①), (⑤), (⑥), (②)). Since the periodic orbit Γ_1^+ in the center is only R_1 -symmetric, this cycle only organizes families of R_1 -symmetric and R_1 -symmetry-broken homoclinic solutions.

Secondly, we consider the heteroclinic cycles given by the edge sequence

$$\mathbf{0} \xrightarrow{\textcircled{3}} \Gamma_1^+ \xrightarrow{\textcircled{6}} \Gamma_* \xrightarrow{\textcircled{5}} \Gamma_1^+/\Gamma_1^- \xrightarrow{\textcircled{4}} \mathbf{0},$$

which are of type ((③), (⑥), (⑤), (④)). Since now the periodic orbit Γ_* at the center is R_* -symmetric, this cycle organizes families of both R_1 - and R_2 -symmetric homoclinic solutions and the corresponding symmetry-broken homoclinic solutions.

For each of these two types of more complex homoclinic solutions to $\mathbf{0}$, we present again representative examples as well as the bifurcation diagram in β_2 with the corresponding branches.

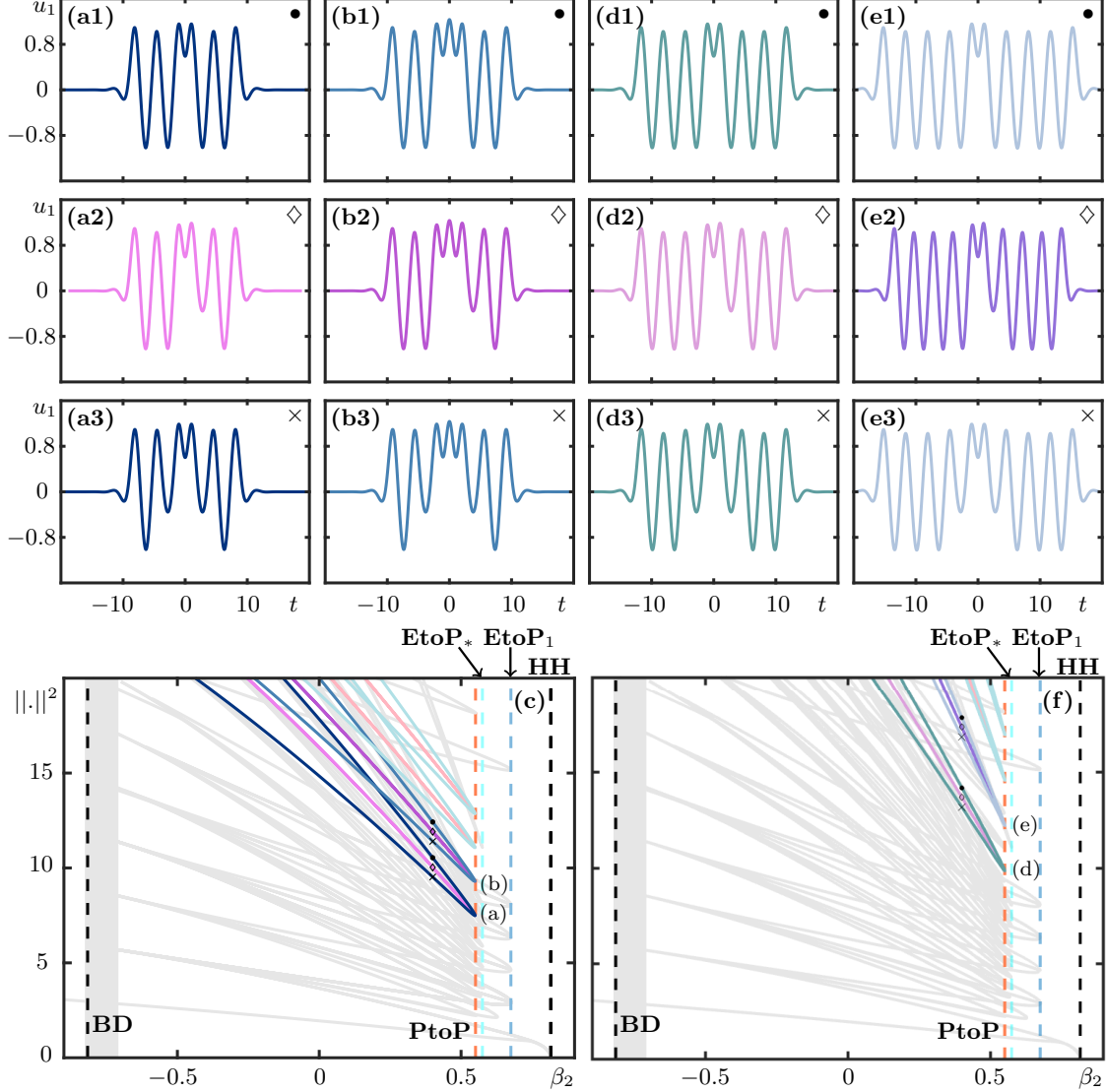


Figure 12: Families of homoclinic solutions to $\mathbf{0}$ of system (2) generated by the EtoP and PtoP connections of the edge sequence $(\textcircled{1}, \textcircled{5}, \textcircled{6}, \textcircled{2})$. Panels (a1),(b1) and (d1),(e1) and (a3),(b3) and (d3),(e3) show R_1 -symmetric, and panels (a2),(b2) and (d2),(e2) R_1 -symmetry-broken homoclinic solutions, all for $\beta_2 = 0.4$. Panels (c) and (f) are the bifurcation diagrams in β_2 of the homoclinic solutions in panels (a) and (b), and of those in panels (d) and (e), respectively. The grey curves are the branches from Figure 6. The vertical dashed lines indicate **BD**, **HH** and the fold points **EtoP***, **EtoP₁** and **PtoP**; the color of the bifurcation curves and the dots, crosses and diamonds indicate the locations of the solutions in panels (a),(b) and (d),(f), respectively.

5.1 Solitons of type $(\textcircled{1}, \textcircled{5}, \textcircled{6}, \textcircled{2})$

Figure 12 shows families of homoclinic solutions to $\mathbf{0}$ for $\beta_2 = 0.4$ that are organized by the heteroclinic cycles with the edge sequence $(\textcircled{1}, \textcircled{5}, \textcircled{6}, \textcircled{2})$. This type is determined by the fact that the connections $\textcircled{6}$ and $\textcircled{2}$ are the R_1 -counterparts of the connections $\textcircled{5}$ and $\textcircled{1}$, respectively. As panels (a),(b) and (d),(f) of Fig. 12 show, multi-oscillation solitons of this type correspond to homoclinic orbits that leave $\mathbf{0}$ to oscillate around Γ_* , transition to oscillate around Γ_1^+ , transition back and oscillate around Γ_* again, and finally return to $\mathbf{0}$. The connections can be made by either of the pair of EtoP from Fig. 4(a) and PtoP connections from Fig. 8(a), and the number of oscillations of each of these episodes differs from branch to branch, as is

illustrated in the bifurcation diagram in Fig. 12(c) and (f).

More specifically, Fig. 12(a1) shows an R_1 -symmetric homoclinic solutions of this type: from $\mathbf{0}$ it follow the EtoP connection in Fig. 5(a2); makes two loops close to Γ_* ; follows the PtoP connection in Fig. 8(a1); makes one loop close to Γ_1^+ ; follows the R_1 -counterpart of the PtoP connection in Fig. 8(a1); makes two loops close to Γ_* ; and finally follows the R_1 -counterpart of the EtoP connection in Fig. 5(a2) back to $\mathbf{0}$. The homoclinic solution in panel (a3) of Fig. 12 differs only in that it follows the PtoP connection in Fig. 8(a2) and its R_1 -counterpart. The homoclinic solution in panel (a2), on the other hand, is R_1 -symmetry-broken, because it first follows the EtoP and PtoP connection in Fig. 5(a2) and Fig. 8(a1), respectively, and then converges back to $\mathbf{0}$ by following the R_1 -counterparts of the PtoP and EtoP connections in Fig. 8(a2) and Fig. 5(a2), respectively. Fixing the number of loops near Γ_* and increasing the number of loops near Γ_1^+ generates families of R_1 -symmetric and R_1 -symmetry-broken homoclinic solutions, and panels (b1), (b2) and (b3) show the ones with one additional loop.

Figure 12(c) shows the bifurcation diagram in β_2 of these families, where solutions are again represented by their L_2 -norm $\|\cdot\|^2$. Here, we show the curves of the homoclinic solutions with two to five loops near Γ_1^+ ; the bifurcations **BD** and **HH** that bound region II are shown by dashed vertical lines, as are the fold points **EtoP***, **EtoP₁** and **PtoP**. For reference, all previously found branches of homoclinic solutions[6] from Sec. 3 are shown in light gray. The two R_1 -symmetric homoclinic solutions in panels (a1) and (a3) of Fig. 12, with the same number of loops near Γ_* and Γ_1^+ , respectively, lie on branches that connect at a fold point to form a smooth curve. As is the case for the simpler homoclinic orbits, this fold is also a point of symmetry breaking from which bifurcates a pair of branches of R_1 -symmetry-broken homoclinic solutions; the one in panel (a2) lies on one of these branches (which coincide because they have the same L_2 -norm). This picture of branches connecting as pairs at joint fold points is repeated in panel (c) when the number of loops near Γ_1^+ is increased; the positions of the homoclinic solutions in panels (b) are indicated on the respective branches.

More families of homoclinic solutions associated with type $(\textcircled{1}, \textcircled{5}, \textcircled{6}, \textcircled{2})$ can be generated by fixing the oscillations near Γ_1^+ and increasing the number of loops near Γ_* . As before, there exist R_1 -symmetric and R_1 -symmetry-broken families of homoclinic solutions, and examples of them are shown in panels (d) and (e) of Fig. 12. Notice that those in panels (d) are like the ones in panels (a), but with one further loop near Γ_* ; similarly, the homoclinic solutions in panels (e) have two extra loops near Γ_* . As the bifurcation diagram in panel (f) shows, all these R_1 -symmetric and R_1 -symmetry-broken homoclinic solutions also lie on a single curve with two branches that meet at a fold point, from which branches of the R_1 -symmetry-broken homoclinic solutions bifurcate.

5.2 Solitons of type $(\textcircled{3}, \textcircled{6}, \textcircled{5}, \textcircled{4})$

Figure 13 shows families of homoclinic solutions to $\mathbf{0}$ that are organized by the heteroclinic cycles with the edge sequence $(\textcircled{3}, \textcircled{6}, \textcircled{5}, \textcircled{4})$. Shown are examples of R_1 -symmetric and R_1 -symmetry-broken homoclinic solutions in panels (a) and (b), and of R_2 -symmetric and R_2 -symmetry-broken homoclinic solutions in panels (a) and (b), respectively; the corresponding bifurcation diagrams in β_2 are shown in panels (c) and (f). For the R_1 -symmetric and R_1 -symmetry-broken homoclinic solutions, the connections $\textcircled{5}$ and $\textcircled{4}$ are the R_1 -counterparts of the connections $\textcircled{6}$ and $\textcircled{3}$, respectively. All these homoclinic solutions loop close to Γ_1^+ before converging back to $\mathbf{0}$. For the R_2 -symmetric and R_2 -symmetry-broken homoclinic solutions, the connections $\textcircled{5}$ and $\textcircled{4}$ are the R_2 -counterparts of the connections $\textcircled{6}$ and $\textcircled{3}$, respectively; so now all these homoclinic solutions loop close to Γ_1^- before converging back to $\mathbf{0}$.

To be more specific, the homoclinic solution in Fig. 13(a1) follows the EtoP connection in Fig. 5(a2) and makes two loops near Γ_1^+ . After that, it follows the R_1 -counterpart of the PtoP connection in Fig. 8(a1) and makes one loop near Γ_* ; subsequently, it follows the PtoP connection in Fig. 8(a1) and the R_1 -counterpart of the EtoP connection in Fig. 5(a1) to converge back to $\mathbf{0}$. Similarly, the homoclinic solution in panels (a3) also makes use of the EtoP connection in Fig. 5(a1); however, it is now associated with the PtoP connection in Fig. 8(a2). The homoclinic solutions in panels (b1) and (b3) are similar to the ones in panels (a1) and (a3), but make one additional loop near Γ_* . The corresponding R_1 -symmetry-broken homoclinic solutions are shown in panels (a2) and (b2), respectively. Similar to what we found in Fig. 12, one can also generate other families of homoclinic solutions by fixing the number of loops they make near Γ_* and by increasing the number of loops near Γ_1^+ . As the bifurcation diagram in Fig. 13(c) shows, all these R_1 -symmetric and R_1 -symmetry-broken homoclinic solutions also lie on a single curve with two branches that meet at a fold

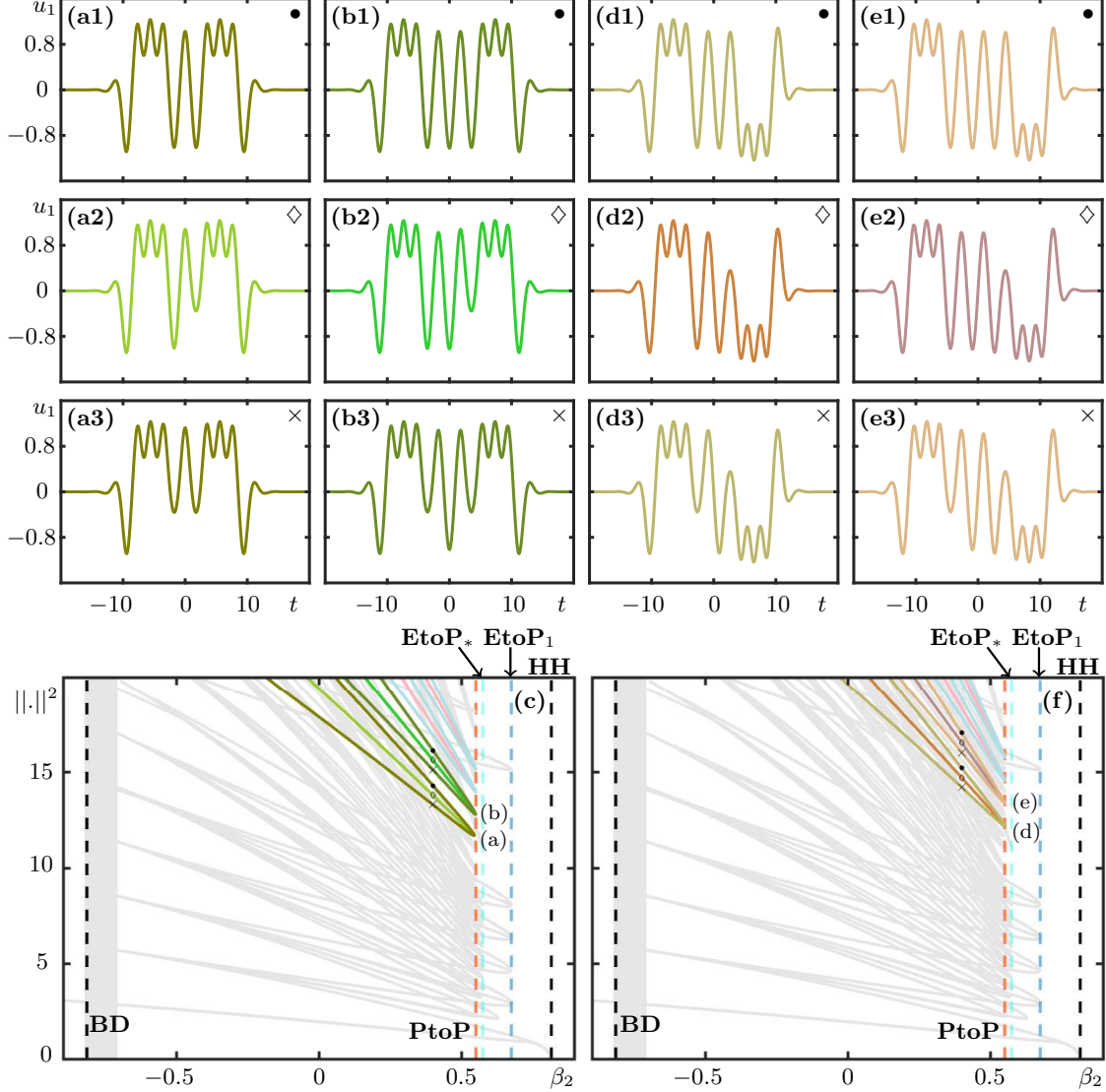


Figure 13: Families of homoclinic solutions to $\mathbf{0}$ of system (2) generated by the EtoP and PtoP connections of the edge sequence $(\textcircled{3}, \textcircled{6}, \textcircled{5}, \textcircled{4})$. Panels (a1),(b1) and (a3),(b3) show R_1 -symmetric, panels (a2),(b2) R_1 -symmetry-broken, panels (d1),(e1) and (d3),(e3) show R_2 -symmetric, and panels (d2),(e2) R_2 -symmetry-broken homoclinic solutions, all for $\beta_2 = 0.4$. Panels (c) and (f) are the bifurcation diagrams in β_2 of the homoclinic solutions in panels (a) and (b), and of those in panels (d) and (e), respectively. The grey curves are the branches from Figure 6. The vertical dashed lines indicate **BD**, **HH** and the fold points **EtoP***, **EtoP₁** and **PtoP**; the color of the bifurcation curves and the dots, crosses and diamonds indicate the locations of the solutions in panels (a),(b) and (d),(f).

point.

It is also possible to generate families of R_2 -symmetric and R_2 -symmetry-broken homoclinic solutions of type $(\textcircled{3}, \textcircled{6}, \textcircled{5}, \textcircled{4})$, and examples are shown in panels (d) and (e) of Fig. 13. As panels (d1),(e1) and (d3),(e3) show, such R_2 -symmetric homoclinic solutions initially loop twice close to Γ_1^+ , then follow the respective PtoP connections to loop close to Γ_* and, finally, loop three times close to Γ_1^- , instead of Γ_1^+ , before returning to $\mathbf{0}$. As before, the corresponding R_2 -symmetry-broken homoclinic solutions can be constructed by combining the two different PtoP connections, and they are shown in panels (d2) and (e2). The difference between the homoclinic orbits in panels (d) and (e) is that they have one and two loops near Γ_* , respectively.

Taking more loops near Γ_* creates additional homoclinic orbits of the respective family, of which the first four are shown in the bifurcation diagram in Fig. 13(f). Also the R_2 -symmetric homoclinic solutions lie in pairs on curves with two branches that meet at fold points, from which branches of the corresponding R_2 -symmetry-broken homoclinic solutions emerge.

5.3 BD-truncated snaking of multi-oscillation solitons

Figures 12 and 13 illustrate the existence of an entire menagerie of additional homoclinic orbits to $\mathbf{0}$ that visit any of the periodic orbits Γ_* and Γ_1^\pm . These additional homoclinic solutions are indeed all multi-oscillation solitons of the GNLSE. More specifically, for any chosen edge sequence, one can find the associated families of symmetric and symmetry-broken homoclinic solutions; these include R_2 -symmetric and R_2 -symmetry-broken ones when the respective heteroclinic cycle is not R_2 -symmetric itself. Figures 12 and 13 show certain families given by increasing only the number of loops near one of the constituent periodic orbits. However, we observe and conjecture that homoclinic solutions exist for any prescribed number of loops near any of the constituent periodic orbits of a given type. Note also that the R_2 -counterparts of the shown homoclinic solutions also exist. We do not show them here because, on the level of the u_1 -traces shown in these figures, they simply correspond to reflections of u_1 in the t -axis, so that maxima become minima and vice versa, and Γ_1^+ and Γ_1^- are exchanged.

As the bifurcation diagrams in panels (c) and (f) of Figs. 12 and 13 illustrate, all these multi-oscillation solitons lie on curves organized by BD-truncated homoclinic snaking. Indeed, in spite of increasing numerical sensitivity due to their more complicated nature, we are able to continue all branches of multi-oscillation solitons for decreasing β_2 to quite near the point **BD** to confirm this. All these solutions require the existence of the respective EtoP and PtoP connections. Since the fold **PtoP** of the latter occurs for smaller β_2 than the folds **EtoP** $_*$, **EtoP** $_1$ of the different EtoP connections, all these multi-oscillation solitons involving the periodic orbits Γ_* and Γ_1^\pm lie on branches that have folds near **PtoP**. In fact, as was also the case for the folds of generalized solitons in Sec. 4, the fold points of multi-oscillation solitons are indistinguishable in their β_2 -value (as found by continuation) from that of the fold **PtoP**.

6 Discussions and outlook

We showed that there exist infinitely many infinite families of generalized and multi-oscillation solitons of the GNLSE, in addition to the families of ‘regular’ solitons that were found before [6]. To achieve this, we used a dynamical system approach to translate solitons of the GNLSE into homoclinic orbits to the equilibrium $\mathbf{0}$ in the zero-energy level of the ODE system (2), which is Hamiltonian and features two reversible symmetries, R_1 and R_2 . The new kinds of solitons crucially involve transitions between periodic solutions, which are given by PtoP connections between saddle-type periodic orbits of the ODE. For the specific example of the primary periodic orbits Γ_* and Γ_1^\pm in the zero-energy level, we showed how PtoP connections between them give rise to infinite families of homoclinic orbits to either of the constituent periodic orbits. In terms of the GNLSE, these solutions are generalized solitons with non-decaying oscillating tails; notably, these PtoP connections and associated generalized solitons are not confined to the zero-energy level. Furthermore, PtoP connections in the zero-energy level can be combined with EtoP connections from $\mathbf{0}$ to the respective periodic orbits into heteroclinic cycles. As we argued, these generate infinite families of homoclinic solutions to $\mathbf{0}$, which are multi-oscillation solitons of the GNLSE with different episodes of oscillations near any of the periodic orbits they visit. We stress that these solitons are not bound states or ‘molecules’ of two or more interacting primary solitons.

All these solitons can be continued in parameters. Specifically, we showed by changing the strength β_2 of the quadratic dispersion that all solitons are organized as BD-truncated homoclinic snaking, even the generalized solitons that correspond to homoclinic solutions to periodic orbits. This means that, for all families of solitons, pairs of branches start at the Belyakov-Daveney bifurcation **BD** and meet at fold bifurcations that are also symmetry-breaking bifurcation of the respective solutions. The folds of a given family accumulate on the folds of the respective EtoP or ProP connections that are organizing it. Note, in particular, that all these solutions of the GNLSE exist for $\beta_2 = 0$, that is, for the case of pure quartic dispersion.

For heteroclinic cycles involving only the equilibrium $\mathbf{0}$ and the primary periodic orbits Γ_* and Γ_1^\pm , we presented a directed graph with numbered edges to encode the possibilities: any edge sequence in this graph from and back to $\mathbf{0}$ generates associated families of multi-oscillation solitons of the respective type. While we supported it only for certain families, it is a natural conjecture that this statement generally holds. What is more, the graph can also be used to construct more complicated generalized solitons by selecting edge sequences of this graph that avoid the equilibrium. However, the story is even more complicated: already the basic surfaces \mathcal{S}_* and \mathcal{S}_1^\pm intersect the zero-energy level infinitely many times as they converge onto the (union of the) primary homoclinic orbits. Hence, the graph we presented can be extended with infinitely more periodic orbits of \mathcal{S}_* and \mathcal{S}_1^\pm and associated edges that represent EtoP connections from $\mathbf{0}$ to them, as well as PtoP connections between all these additional periodic orbits. We conjecture that any edge sequence in this much extended graph also generates families of multi-oscillation solitons of the corresponding type, as was shown for the cases presented here. But there is even more: any of the thus created solitons is itself the limit of a family of periodic orbits! We suspect that each of them, when continued in the energy, creates infinitely many periodic orbits in the zero-energy level that also feature EtoP and PtoP connections, and so on. The picture that emerges is truly a never-ending and ‘self-similar’ plethora of additional solitons, which we conjecture are all created at the point **BD** as part of the overall phenomenon of BD-truncated homoclinic snaking of the ODE system (2) and, hence the GNLSE (1). More generally, we conjecture that a Belyakov-Devaney bifurcation in any fourth-order Hamiltonian system with two reversible symmetries is an organizing center near which all of the solutions reported here can be found in the same way.

There are certainly avenues for future research that arise from our study. First of all, we already alluded to the geometry of the basic surfaces \mathcal{S}_* and \mathcal{S}_1^\pm , which we only considered here for the fixed parameter value $\beta_2 = 0.4$. As β_2 is increased, these surfaces interact and their different parts connect differently in a sequence of transitions through specific types of symmetry-breaking bifurcations, period- k multiplying bifurcations, and saddle-node bifurcations; these results will be presented elsewhere [7]. Secondly, it remains a considerable challenge to formally prove the existence of the EtoP and PtoP connections and all the different families of homoclinic orbits they generate, presumably starting with the specific ones we already found by numerical continuation. This could possibly be done by setting up Lin’s method as a theoretical tool (rather than a numerical one) [33, 26]. Moreover, our computations based on boundary-value problem formulations come with error bounds; hence, the existence of any connecting orbit we showed here can be proved, in principle, in a computer-assisted way [40, 24]. Another issue is the stability of the different solitons as solutions of the PDE. Only the primary single-hump soliton is stable [37, 39], while all the other solitons we discovered appear to be unstable (but some are only weakly unstable [6]). Establishing this observation rigorously remains a considerable challenge for future work and will require state-of-the art techniques, such as the computation of Evans functions [8].

Finally, localized structures in other spatially extended systems may be studied and explored, in the same spirit, with the numerical continuation approach employed here. In particular, recent experiments [36] have shown the feasibilities of creating waveguides with higher even-order dispersions, which are described by further generalizations of the NLSE with corresponding non-zero dispersion terms of order six, eight, ten, or even higher. Other examples of interesting PDEs in this context are the widely studied class of the NLSE describing solitary wave formation in inhomogeneous media [29, 27, 19, 28], and the Lugiato-Lefever equation [34], which both are known to feature homoclinic snaking.

Acknowledgments

A. Giraldo was supported by KIAS Individual Grant No. CG086101 at the Korea Institute for Advanced Study.

Data availability

The data that support the findings of this study are available from the corresponding author upon reasonable request.

References

- [1] N. N. Akhmediev, A. V. Buryak, and M. Karlsson. Radiationless optical solitons with oscillating tails. *Opt. Commun.*, 110(5):540 – 544, 1994.
- [2] N. N. Akhmediev and A. V. Buryak. Interactions of solitons with oscillating tails. *Opt. Commun.*, 121(4):109 – 114, 1995.
- [3] T. J. Alexander, G. A. Tsolias, A. Demirkaya, R. J. Decker, C. M. De Sterke, and P. G. Kevrekidis. Dark solitons under higher-order dispersion. *Opt. Lett.*, 47(5):1174–1177, Mar 2022.
- [4] C. J. Amick and J. F. Toland. Homoclinic orbits in the dynamic phase-space analogy of an elastic strut. *Eur. J. Appl. Math.*, 3(2):97–114, 1992.
- [5] S. Bakrani, J. S. W. Lamb, and D. Turaev. Invariant manifolds of homoclinic orbits and the dynamical consequences of a super-homoclinic: a case study in (\mathbb{R}^4) with (\mathbb{Z}_2) -symmetry and integral of motion, 2021.
- [6] R. I. Bandara, A. Giraldo, N. G. R. Broderick, and B. Krauskopf. Infinitely many multipulse solitons of different symmetry types in the nonlinear Schrödinger equation with quartic dispersion. *Phys. Rev. A*, 103:063514, Jun 2021.
- [7] R. I. Bandara, A. Giraldo, N. G. R. Broderick, and B. Krauskopf. Surfaces of period orbits and their bifurcations in the nonlinear Schrödinger equation with quartic dispersion. *Preprint in preparation*, 2023.
- [8] B. Barker, J. Humpherys, G. Lyng, and J. Lytle. Evans function computation for the stability of travelling waves. *Phil. Trans. R. Soc. A.*, 376(2117):20170184, 2018.
- [9] A. Blanco-Redondo, C. M. De Sterke, J. E. Sipe, T. F. Krauss, B. J. Eggleton, and C. Husko. Pure-quartic solitons. *Nat. Commun.*, 7:10427, 2016.
- [10] J. Burke and E. Knobloch. Snakes and ladders: Localized states in the Swift-Hohenberg equation. *Phys. Lett. A*, 360:681–688, 01 2007.
- [11] A. R. Champneys. Homoclinic orbits in reversible systems and their applications in mechanics, fluids and optics. *Physica D*, 112(1-2):158–186, 1998.
- [12] A. R. Champneys. Homoclinic orbits in reversible systems II: Multi-bumps and saddle-centres. *CWI Quarterly*, 12:185–212, 01 1999.
- [13] A. R. Champneys, Y. A. Kuznetsov, and B. Sandstede. A numerical toolbox for homoclinic bifurcation analysis. *Internat. J. Bifur. Chaos Appl. Sci. Engrg.*, 6(05):867–887, 1996.
- [14] A. R. Champneys and A. Spence. Hunting for homoclinic orbits in reversible systems: a shooting technique. *Adv. Comput. Math.*, 1(1):81–108, 1993.
- [15] A. R. Champneys and J. F. Toland. Bifurcation of a plethora of multi-modal homoclinic orbits for autonomous Hamiltonian systems. *Nonlinearity*, 6(5):665, 1993.
- [16] R. L. Devaney. Reversible diffeomorphisms and flows. *Trans. Amer. Math. Soc.*, 218:89–113, 1976.
- [17] R. L. Devaney. Blue sky catastrophes in reversible and Hamiltonian systems. *Indiana Univ. Math. J.*, 26(2):247–263, 1977.
- [18] E. J. Doedel and B. E. Oldeman. *AUTO-07p: Continuation and Bifurcation Software for Ordinary Differential Equations*. Department of Computer Science, Concordia University, Montreal, Canada, 2010. With major contributions from A. R. Champneys, F. Dercole, T. F. Fairgrieve, Y. Kuznetsov, R. C. Paffenroth, B. Sandstede, X. J. Wang and C. H. Zhang; available at <http://www.cmv1.cs.concordia.ca/>.
- [19] K. Dragonas and Y. Kominis. Solitary wave formation under the interplay between spatial inhomogeneity and nonlocality. *Phys. Rev. E*, 100:052209, Nov 2019.

- [20] A. J. Elvin, C. R. Laing, R. I. McLachlan, and M. G. Roberts. Exploiting the Hamiltonian structure of a neural field model. *Physica D*, 239(9):537 – 546, 2010.
- [21] J. Galan-Vioque, F. J. M. Almaraz, and E. F. Macías. Continuation of periodic orbits in symmetric Hamiltonian and conservative systems. *Eur. Phys. J. Top.*, 223(13):2705–2722, 2014.
- [22] A. J. Homburg and J. S. W. Lamb. Symmetric homoclinic tangles in reversible systems. *Ergod. Theory Dyn. Syst.*, 26(6):1769–1789, 2006.
- [23] A. J. Homburg and B. Sandstede. Homoclinic and heteroclinic bifurcations in vector fields. In H.W. Broer, B. Hasselblatt, and F. Takens, editors, *Handbook of Dynamical Systems, volume 3*, pages 379–524. Elsevier Amsterdam, 2010.
- [24] T. Kapela, M. Mrozek, D. Wilczak, and P. Zgliczyński. CAPD:: DynSys: a flexible C++ toolbox for rigorous numerical analysis of dynamical systems. *Communications in Nonlinear Science and Numerical Simulation*, 101:105578, 2021.
- [25] M. Karlsson and A. Höök. Soliton-like pulses governed by fourth order dispersion in optical fibers. *Opt. Commun.*, 104(4-6):303–307, 1994.
- [26] J. Knobloch, J. S. W. Lamb, and K. N Webster. Using Lin’s method to solve Bykov’s problems. *Differ. Equ.*, 257(8):2984–3047, 2014.
- [27] Y. Kominis. Bright, dark, antidark, and kink solitons in media with periodically alternating sign of nonlinearity. *Phys. Rev. A*, 87:063849, Jun 2013.
- [28] Y. Kominis, J. Cuevas-Maraver, P. G. Kevrekidis, D. J. Frantzeskakis, and A. Bountis. Continuous families of solitary waves in non-symmetric complex potentials: A Melnikov theory approach. *Chaos, Solitons & Fractals*, 118:222–233, 2019.
- [29] Y. Kominis and K. T. Hizanidis. Power dependent soliton location and stability in complex photonic structures. *Opt. Express*, 16(16):12124–12138, Aug 2008.
- [30] B. Krauskopf, H. M. Osinga, and J. Galán-Vioque. *Numerical Continuation Methods for Dynamical Systems*. Springer, 2007.
- [31] B. Krauskopf and T. Rieß. A Lin’s method approach to finding and continuing heteroclinic connections involving periodic orbits. *Nonlinearity*, 21(8):1655, 2008.
- [32] J. J. Palis and W. De Melo. *Geometric Theory of Dynamical Systems: An Introduction*. Springer Science & Business Media, 2012.
- [33] R. Parker and A. Aceves. Multi-pulse solitary waves in a fourth-order nonlinear Schrödinger equation. *Physica D: Nonlinear Phenomena*, 422:132890, 2021.
- [34] P. Parra-Rivas, D. Gomila, L. Gelens, and E. Knobloch. Bifurcation structure of localized states in the Lugiato-Lefever equation with anomalous dispersion. *Phys. Rev. E*, 97, 01 2018.
- [35] S. Roy and F. Biancalana. Formation of quartic solitons and a localized continuum in silicon-based slot waveguides. *Phys. Rev. A*, 87:025801, Feb 2013.
- [36] A. F. J. Runge, Y. L. Qiang, T. J. Alexander, M. Z. Rafat, D. D. Hudson, A. Blanco-Redondo, and C. M. de Sterke. Infinite hierarchy of solitons: Interaction of Kerr nonlinearity with even orders of dispersion. *Phys. Rev. Research*, 3:013166, Feb 2021.
- [37] K. K. K. Tam, T. J. Alexander, A. Blanco-Redondo, and C. M. De Sterke. Solitary wave solutions in nonlinear media with quartic and quadratic dispersion-implications for high-power lasers. In *Laser Science*, pages JW4A–78. Optical Society of America, 2018.
- [38] K. K. K. Tam, T. J. Alexander, A. Blanco-Redondo, and C. M. De Sterke. Stationary and dynamical properties of pure-quartic solitons. *Opt. Lett.*, 44(13):3306–3309, 2019.

- [39] K. K. K. Tam, T. J. Alexander, A. Blanco-Redondo, and C. M. De Sterke. Generalized dispersion Kerr solitons. *Phys. Rev. A*, 101:043822, Apr 2020.
- [40] D. Wilczak and P. Zgliczyński. Heteroclinic connections between periodic orbits in planar restricted circular three-body problem — a computer assisted proof. *Communications in Mathematical Physics*, 234:37–75, 2003.
- [41] P. D. Woods and A. R. Champneys. Heteroclinic tangles and homoclinic snaking in the unfolding of a degenerate reversible Hamiltonian–Hopf bifurcation. *Physica D*, 129(3-4):147–170, 1999.